

1 **The Innovative Strategies for Observations in the Arctic Atmospheric**
2 **Boundary Layer Project (ISOBAR) — Unique fine-scale observations under**
3 **stable and very stable conditions**

4 Stephan T. Kral*

5 *Geophysical Institute and Bjerknes Centre for Climate Research, University of Bergen, Bergen,*
6 *Norway*

7 Joachim Reuder

8 *Geophysical Institute and Bjerknes Centre for Climate Research, University of Bergen, Bergen,*
9 *Norway*

10 Timo Vihma

11 *Finnish Meteorological Institute, Helsinki, Finland*

12 Irene Suomi

13 *Finnish Meteorological Institute, Helsinki, Finland*

14 Kristine Flacké Hualand

15 *Geophysical Institute and Bjerknes Centre for Climate Research, University of Bergen, Bergen,*
16 *Norway*

17 Gabin H. Urbancic

18 *Geophysical Institute, University of Bergen, Bergen, Norway, and Finnish Meteorological*
19 *Institute, Helsinki, Finland*

20 Brian R. Greene

21 *School of Meteorology, Advanced Radar Research Center, and Center for Autonomous Sensing*
22 *and Sampling, University of Oklahoma, Norman, Oklahoma, USA*

23 Gert-Jan Steeneveld

24 *Meteorology and Air Quality Section, Wageningen University, Wageningen, Netherlands*

25 Torge Lorenz

26 *NORCE Norwegian Research Centre and Bjerknes Centre for Climate Research, Bergen, Norway*

27 Björn Maronga

28 *Institute of Meteorology and Climatology, Leibniz University Hannover, Hannover, Germany, and*
29 *Geophysical Institute, University of Bergen, Bergen, Norway*

30 Marius O. Jonassen

31 *The University Centre in Svalbard, Longyearbyen, Norway and Geophysical Institute, University*
32 *of Bergen, Bergen, Norway*

33 Hada Ajosenpää

34 *Finnish Meteorological Institute, Helsinki, Finland*

35 Line Båserud

36 *Geophysical Institute and Bjerknes Centre for Climate Research, University of Bergen, Bergen,*
37 *Norway, and Norwegian Meteorological Institute, Oslo, Norway*

38
39
40
41
42
43
44
45
46
47
48
49
50
51
52
53
54
55
56

Phillip B. Chilson

*School of Meteorology, Advanced Radar Research Center, and Center for Autonomous Sensing
and Sampling, University of Oklahoma, Norman, Oklahoma, USA*

Albert A. M. Holtslag

Meteorology and Air Quality Section, Wageningen University, Wageningen, Netherlands

Alastair D. Jenkins

Geophysical Institute, University of Bergen, Bergen, Norway

Rostislav Kouznetsov

*Finnish Meteorological Institute, Helsinki, Finland, and Obukhov Institute for Atmospheric
Physics, Moscow, Russia*

Stephanie Mayer

NORCE Norwegian Research Centre and Bjerknes Centre for Climate Research, Bergen, Norway

Elizabeth A. Pillar-Little

*School of Meteorology and Center for Autonomous Sensing and Sampling, University of
Oklahoma, Norman, Oklahoma, USA*

Alexander Rautenberg

Center for Applied Geoscience, Eberhard-Karls-Universität Tübingen, Tübingen, Germany

Johannes Schwenkel

Institute of Meteorology and Climatology, Leibniz University Hannover, Hannover, Germany

57

Andrew W. Seidl

58

Geophysical Institute and Bjerknes Centre for Climate Research, University of Bergen, Bergen,

59

Norway

60

Burkhard Wrenger

61

Ostwestfalen-Lippe University of Applied Sciences and Arts, Höxter, Germany

⁶² *Corresponding author: Stephan T. Kral, stephan.kral@uib.no

ABSTRACT

63 The Innovative Strategies for Observations in the Arctic Atmospheric Boundary Layer Program
64 (ISOBAR) is a research project investigating stable atmospheric boundary layer (SBL) processes,
65 whose representation still poses significant challenges in state-of-the-art numerical weather pre-
66 diction (NWP) models. In ISOBAR ground-based flux and profile observations are combined with
67 boundary-layer remote sensing methods and the extensive usage of different unmanned aircraft
68 systems (UAS). During February 2017 and 2018 we carried out two major field campaigns over
69 the sea ice of the northern Baltic Sea, close to the Finnish island of Hailuoto at 65 °N. In total
70 14 intensive observational periods (IOPs) resulted in extensive SBL datasets with unprecedented
71 spatiotemporal resolution, which will form the basis for various numerical modeling experiments.
72 First results from the campaigns indicate numerous very stable boundary layer (VSBL) cases,
73 characterized by strong stratification, weak winds, and clear skies, and give detailed insight in the
74 temporal evolution and vertical structure of the entire SBL. The SBL is subject to rapid changes in
75 its vertical structure, responding to a variety of different processes. In particular, we study cases
76 involving a shear instability associated with a low-level jet, a rapid strong cooling event observed
77 a few meters above ground, and a strong wave-breaking event that triggers intensive near-surface
78 turbulence. Furthermore, we use observations from one IOP to validate three different atmo-
79 spheric models. The unique fine-scale observations resulting from the ISOBAR observational
80 approach will aid future research activities, focusing on a better understanding of the SBL and its
81 implementation in numerical models.

82 *Capsule summary.* Combining ground-based micrometeorological instrumentation with bound-
83 ary layer remote sensing and unmanned aircraft systems for high-resolution observations on the
84 stable boundary layer over sea ice and corresponding modelling experiments.

85 **Background and Motivation**

86 The stably-stratified atmospheric boundary layer (SBL) is common in the Arctic, where the
87 absence of solar radiation during winter causes a negative net radiation at the surface. Even during
88 daylight seasons, the high surface albedo of snow and ice favors SBL formation (Persson et al.
89 2002). The SBL is of particular interest for our understanding of the Arctic climate system (e.g.,
90 Bintanja et al. 2012; Lesins et al. 2012; Davy and Esau 2016), which experiences a significantly
91 stronger warming than the rest of the globe, commonly referred to as Arctic Amplification (Serreze
92 et al. 2009; Serreze and Barry 2011; Pithan and Mauritsen 2014; Dai et al. 2019). The state of
93 and the processes in the ABL affect the turbulent and radiative heat fluxes from the atmosphere
94 to the Earth's surface and, accordingly, the surface mass balance of sea ice, ice sheets, glaciers,
95 and terrestrial snow. Hence, the correct understanding and parameterization of the SBL and its
96 coupling to the underlying snow, ice, or land surface is crucial for the reliability of climate model
97 projections in polar regions. Another strong indication for the importance of the SBL is the fact
98 that the observed global warming trend over the last decades is most pronounced at nighttime and
99 in polar regions, both when SBL prevail (McNider et al. 2010).

100 Climate and numerical weather prediction (NWP) models suffer from insufficient ABL param-
101 eterizations and have a strong need for an improved representation of the SBL, in particular in
102 very stable boundary layer (VSBL) conditions. This is demonstrated by large errors under VSBL
103 conditions, where 2-m air temperature errors (ΔT_{2m}) of the order of 10 K are common even in
104 short-term (24-h) NWP products (Atlaskin and Vihma 2012). In atmospheric reanalyses, broadly

105 applied in diagnostics of climate variability and change, the monthly/seasonal means of ΔT_{2m} in
106 the Arctic (Jakobson et al. 2012; Graham et al. 2019) and Antarctic (Jonassen et al. 2019) typ-
107 ically show values of a few kelvins, and can even reach 20 K, strongly depending on the VSBL
108 parameterization applied (Uppala et al. 2005). The common positive temperature biases are typ-
109 ically related to excessively large downward sensible heat flux (Cuxart et al. 2005; Tjernström
110 et al. 2005), whereas large negative biases may be generated via thermal decoupling between the
111 atmosphere and the snow/ice surface (Mahrt 2003; Uppala et al. 2005). In addition to problems
112 in the turbulence parameterization, most climate models use a too coarse vertical resolution for an
113 appropriate representation of the VSBL (Byrkjedal et al. 2007).

114 The numerical models used for weather prediction and climate scenarios rely on turbulence
115 closure and surface-layer exchange schemes based on Monin-Obukhov similarity theory (MOST,
116 Monin and Obukhov 1954), which relates the non-dimensional vertical gradients of wind, temper-
117 ature and humidity to their respective surface fluxes. MOST is, however, theoretically only valid
118 for stationary, homogeneous flow fields in the atmospheric surface layer, where variations of the
119 turbulent fluxes with height can be neglected. Because the SBL rarely satisfies these conditions,
120 there is substantial need for improvement in the description, characterization, and parameterization
121 of the relevant SBL processes. Moreover, empirical studies evaluating MOST commonly indicate
122 an inability to differentiate between near-neutral and very stable regimes (Foken 2006; Sorbjan and
123 Grachev 2010; Sorbjan 2010; Grachev et al. 2013), which this is largely related to the very weak
124 turbulent heat fluxes present in both situations.

125 The motivation of the Innovative Strategies for Observations in the Arctic Atmospheric Boundary
126 Layer (ISOBAR) project is to improve our understanding of the SBL by applying new observation
127 techniques and numerical modelling experiments, based on the collected data. In combination with
128 well-established ground-based micrometeorological instrumentation and boundary layer remote

129 sensing, we utilize multiple unmanned aircraft systems (UAS) — designed for boundary layer
130 observations — to intensively sample the SBL over sea ice. Through this endeavor, we aim
131 to advance our understanding of the myriad of different processes relevant under very stable
132 stratification. The potential of such observational approaches has been emphasised in a number
133 of SBL review articles (e.g., Fernando and Weil 2010; Mahrt 2014). In particular, we investigate
134 the role of wave–turbulence interaction, the formation and variability of low-level jets (LLJ),
135 intermittency, the spatiotemporal evolution of the SBL structure, and interaction between the SBL
136 and the free atmosphere.

137 The atmospheric boundary layer (ABL) is in general characterized by turbulence generated by
138 wind shear that is either enhanced or suppressed by buoyancy effects, with surface friction and
139 surface heating or cooling as the main drivers. SBL formation is favoured by clear sky and
140 weak wind conditions, typically associated with high pressure synoptic situations characterized by
141 large-scale subsidence and weak pressure gradients. Warm air advection may also contribute to
142 the formation or strengthening of a SBL. In SBL research, it is common to distinguish between
143 the weakly stable boundary layer (WSBL), where turbulence is still the dominating process, and
144 the VSBL, in which turbulence is weak or intermittent. Transitions between WSBL and VSBL
145 take place under clear skies when the net radiative heat loss at the surface becomes larger than
146 the maximum turbulent heat flux that can be maintained by wind shear (de Wiel et al. 2017). As
147 turbulence in the VSBL is typically weak, other processes — such as radiation divergence, surface
148 coupling, wave phenomena, and fog — may become more important. If present, the turbulence is
149 often intermittent.

150 Hoch et al. (2007), Steeneveld et al. (2010) and Gentine et al. (2018) address the substantial
151 role of radiation divergence on the temperature budget under these conditions. Moreover, the
152 lack of turbulent drag in the VSBL coincides with the emergence of LLJ. Bosveld et al. (2014)

153 showed that even for a relatively straightforward LLJ event at Cabauw (The Netherlands), different
154 single-column models (SCM) represent this event rather differently and with considerable biases
155 compared to observations. In addition, gravity waves might propagate under stratified conditions
156 and transport momentum vertically (Nappo 2012; Lapworth and Osborne 2019). The sheer number
157 of involved processes, and their often local nature, results in a rather poor understanding of the SBL
158 in general (Mahrt 2014). An improved understanding of the SBL archetypes and their evolution
159 is in particular hampered by the lack of available vertical profile observations of temperature,
160 humidity and wind speed at an appropriate vertical resolution and at high enough sampling rates,
161 as these variables may vary strongly in time and space.

162 In the WSBL, turbulence can be properly scaled following the local scaling hypothesis proposed
163 by Nieuwstadt (1984), an extension of the original MOST. For the VSBL, classical scaling relations
164 break down and a comprehensive theory is virtually absent. Previous studies successfully applied
165 gradient-based scaling as a function of the gradient Richardson number, Ri (Sorbjan and Grachev
166 2010; Sorbjan 2010). This method is formally equivalent to MOST, but does not suffer from poorly
167 defined scaling parameters (i.e., fluxes that are particularly difficult to measure in the VSBL) and
168 it is also not affected by self-correlation (Sorbjan and Grachev 2010).

169 Further insights into the SBL are crucial for further progress in climate modelling and NWP
170 (Holtslag et al. 2013). Atmospheric circulation models tend to require more drag at the surface
171 than can be justified from local field observations on drag due to vertical shear (Beare 2007;
172 Svensson and Holtslag 2009). This may be due to differences between processes captured by local
173 observations and those acting on the scale of a grid cell, in particular over complex terrain with
174 additional drag resulting from horizontal shear (Goger et al. 2018) or gravity waves (Steenefeld
175 et al. 2008). Without the enhanced drag, the predicted weather systems are typically too persistent.
176 Hence, climate and NWP models have utilized a so-called enhanced mixing approach (Louis 1979)

177 for decades. This approach comes, however, at the cost of the representation of the SBL that is
178 often too warm near the surface, too deep, and the modelled LLJ are often "diluted". This has large
179 consequences for applications such as air quality modelling (Fernando and Weil 2010), road state
180 forecasting (Karsisto et al. 2017), wind energy production (Heppelmann et al. 2017) and visibility
181 forecasts for aviation (Román-Cascón et al. 2019). In climate models, enhanced mixing may result
182 in a positive surface temperature bias (Holtslag et al. 2013), increasing the upwelling longwave
183 radiation (temperature feedback) and decreasing the reflected shortwave radiation through enhanced
184 snow and ice melt (albedo feedback). To overcome the shortcomings of the enhanced mixing
185 approach without impacting the model performance on larger scales, future SBL parameterizations
186 would have to take into account all sources of mechanical drag, for which detailed observations are
187 essential.

188 A number of earlier field campaigns have been dedicated to SBL studies, either over mid-latitude
189 grass fields, such as CASES-99 in Kansas (Poulos et al. 2002) and SABLES 98 in Spain (Cuxart
190 et al. 2000); in hilly terrain with a focus on mountain weather, such as MATERHORN in Utah
191 (Fernando et al. 2015); or in polar regions such as SHEBA in the Arctic Ocean (Uttal et al.
192 2002). These studies provided a wealth of observational data and their analysis offered highly
193 valuable insights into SBL behavior. All these campaigns were, however, limited by their in-
194 situ measurements being from rather low meteorological masts and with supporting atmospheric
195 profiling, e.g., by radiosondes, having rather poor temporal resolution. The availability of new
196 instruments, observation techniques and measurement platforms for probing the SBL, UAS in
197 particular, now offers unique and unrivaled opportunities for a new generation of polar SBL
198 observations (Kral et al. 2018).

199 The application of unmanned, at that time remotely controlled, aircraft for atmospheric research,
200 started at the end of the 1960s. Konrad et al. (1970) used a commercially available hobby model

201 airplane with a wingspan of around 2.5 m to measure profiles of temperature and humidity up to
202 3 km above ground. About two decades later, more systematic attempts for atmospheric investi-
203 gations were conducted, mainly based on relatively large military drones modified for scientific
204 applications (Langford and Emanuel 1993; Stephens et al. 2000). A breakthrough on the path
205 towards smaller and more cost-efficient systems was the Aerosonde, with a wingspan of 2.9 m, an
206 overall take-off weight of 15 kg, and about 5 kg of scientific payload capacity (Holland et al. 2001).

207 A rapid development of small airframes, autopilots and meteorological sensors from around 2000
208 is the direct result of the substantial progress in micro-electronics and component miniaturization.
209 One of the pioneering attempts was the still remotely-controlled system Kali that performed more
210 than 150 flights in Nepal and Bolivia to investigate thermally driven flows in the Himalayas and
211 the Andes (Egger et al. 2002, 2005). During the following decade, a number of different research
212 groups developed small meteorological UAS systems with the aim of providing reasonably priced
213 airborne sensing capabilities for boundary layer research. Some of the most prominent examples
214 are SUMO (Small Unmanned Meteorological Observer, Reuder et al. 2009), M²AV (Meteorological
215 Mini Aerial Vehicle, Spiess et al. 2007), MASC (Multi-purpose Airborne Sensor Carrier, Wildmann
216 et al. 2014), Smartsonde (Chilson et al. 2009; Bonin et al. 2013), and Pilatus (de Boer et al. 2015).
217 A comprehensive overview of small UAS for atmospheric research can be found in Elston et al.
218 (2015).

219 Many ABL campaigns have relied on UAS based data sampling (e.g., Houston et al. 2012;
220 Reuder et al. 2012b; Bonin et al. 2013; Lothon et al. 2014; Reuder et al. 2016; de Boer et al.
221 2019). Several of the aforementioned systems have also been operated successfully in polar
222 environments and provided unique profiles of basic meteorological parameters that have been used
223 for process studies (Curry et al. 2004; Cassano et al. 2010; Cassano 2013; Knuth and Cassano
224 2014; Jonassen et al. 2015; de Boer et al. 2018), meso-scale model validation (Mayer et al. 2012b,c)

225 and the evaluation of the benefit of UAS data assimilation (Jonassen et al. 2012; Sun et al. 2020).
226 However, as fixed-wing systems, they have shortcomings and limitations with respect to accurate
227 measurements in the stable surface layer close to the ground. Rotary-wing multi-copter systems,
228 with their ability to hover and to slowly ascend and descend vertically, have here clear advantages
229 (Neumann and Bartholmai 2015; Palomaki et al. 2017; Wrenger and Cuxart 2017; Bell et al. 2020;
230 Segales et al. 2020).

231 On the basis of previous field campaigns, it is evident that the SBL is often highly heterogeneous
232 over a variety of horizontal scales (e.g., Martínez et al. 2010; Cuxart et al. 2016). Hence, we have
233 to question the classical assumption that sampling over time at one point is equivalent to sampling
234 instantly in space. Accordingly, there is a need for the use of mobile sensor platforms, allowing for
235 observations over a broad range of spatial scales. In ISOBAR we respond to this need by operating
236 a variety of UAS with different capabilities, supported by point and profile observations.

237 **The ISOBAR17 and ISOBAR18 field campaigns**

238 As an integral part of the ISOBAR project, we carried out two field campaigns over the sea ice
239 of the northern Baltic Sea close to the Finnish island Hailuoto in February 2017 and 2018 (see
240 Table 1 for a list of all participants). Hailuoto is located in the Bothnian Bay, the northernmost
241 part of the Baltic Sea, about 20 km west of the city of Oulu (Figure 1). It covers roughly 200 km²,
242 with its highest point reaching only about 20 masl. Our field site was located at 65.037°N and
243 24.555°E, just off-shore of Hailuoto Marjaniemi, the westernmost point of the island, which is
244 also the location of a WMO weather station, operated by the Finnish Meteorological Institute
245 (FMI). Besides the solid sea ice conditions that can be expected for the Bothnian Bay in February
246 (Uotila et al. 2015), the daylight periods are still relatively short, favoring the VSBL development.
247 In addition, this field site provided a solid infrastructure, easy access and the Finnish air traffic

248 regulations allowed for an unbureaucratic flight permission process that enabled very flexible and
249 science-driven UAS operations during the two campaigns.

250 The observational setup largely relied on micrometeorological masts installed on the sea ice, a
251 few hundred meters southwest of the FMI weather station (Figure 1). In 2017 we installed a 4-m
252 mast on the sea ice, equipped with one eddy-covariance (EC) system, three levels of slow-response
253 instrumentation, net radiation and its components (upward and downward for both solar shortwave
254 and thermal longwave radiation), and two ground heat flux sensors. This setup was extended in
255 2018 by erecting a 10-m mast (referred to as GFI2), equipped with the same set of sensors and
256 two additional EC systems. An additional 2-m mast (GFI1), consisting of an EC system and
257 a net radiometer, was placed about 65 m to the north-northwest of the 10-m mast. The nearby
258 WMO station provides observations of temperature, humidity, pressure, cloud base height, cloud
259 fraction, visibility, and precipitation every 10 min at the height of 2 m agl and observations of wind
260 speed, direction and sonic temperature at the height of 46 m asl. Details on station location, sensor
261 placement and specifications for the two campaigns and the different automatic weather stations
262 are summarized in Table 2.

263 For continuous observations of the vertical wind profile and the turbulent structure of the lower
264 atmosphere, we deployed a number of different ABL remote sensing systems: a vertically point-
265 ing 1D LATAN-3M sodar in 2017 and 2018 (Kouznetsov 2009; Kral et al. 2018), a Leosphere
266 WindCube 100S (WC100s) scanning wind lidar in 2017 (Kumer et al. 2014; Kral et al. 2018), a
267 3D Scintec MFAS phased array sodar in 2018, and a 3D Leosphere WindCube v1 (WCv1) doppler
268 wind lidar in 2018 (Kumer et al. 2014, 2016). Table 3 provides an overview of the specifications
269 of these systems and the observed variables.

270 Complementing the observations from the stationary systems, we made intensive use of a number
271 of meteorological UAS, in order to sample profiles of the most important thermodynamic and

272 dynamic properties of the ABL and the lower free atmosphere. A summary of the different UAS
273 and their specifications with corresponding references is given in Table 4 and Figure 2. The three
274 UAS shown in Figure 2 but not listed in Table 4 were still at an experimental stage and their data
275 were not shown in this article.

276 For atmospheric profiles of temperature, humidity and wind up to 1800 m (just below flight level
277 65, our altitude operation limit defined by the aviation authorities) we used the fixed-wing system
278 SUMO, with repeated profiles every 3 h to 4 h during intensive observational periods (IOPs).
279 Multi-copter profiles based on the Bebop2Met (abbreviated B2M), Q13 and CopterSonde (CS)
280 were carried out roughly every 15 min to 30 min during IOPs to gain profiles of the lowermost
281 200 m to 300 m at high vertical resolution. To capture prevailing strong gradients within the
282 SBL, we operated the multi-copters at fairly low climb rates between 0.5 ms^{-1} and 1 ms^{-1} . The
283 second fixed-wing UAS, MASC-2/3, measured turbulence properties along horizontal straight legs
284 at fixed altitudes between 10 m and 425 m, vertically separated by 10 m to 25 m. An overview
285 of the different IOPs, including a basic description of the observed conditions and the number of
286 performed UAS flights is given in Table 5.

287 Post-processing including thorough quality checks resulted in two extensive datasets on the SBL
288 over sea-ice. The overall data availability (see Figure 3 for an overview for the different systems)
289 was significantly improved for ISOBAR18 compared to the previous year. UAS data availability
290 during the first days of the campaigns is very limited since the preparation of the UAS was started
291 after the installation of most ground-based systems was finished. The UOWL team operating the
292 Q13 UAS could not participate for the full campaign period and decided to focus on the last week
293 of ISOBAR17 and the last two weeks of ISOBAR18. In addition, the Bebop2Met (in 2017) and the
294 CopterSonde (in 2018) were operated for the first time during a scientific campaign and required
295 extensive preparation, resulting in limited data availability from these UAS during approximately

296 the first week of the corresponding campaign. Furthermore, icing on the inside of the WindCube
297 100S lense (in 2017) and the late arrival of the WindCube v1 (in 2018) caused the major data gaps
298 in the remotely sensed wind profiles.

299 **Meteorological and sea ice conditions**

300 ISOBAR17 was exposed to varying weather conditions (Figure 4a). Around the start of the
301 campaign, a large high pressure pattern strengthened over Finland, resulting in a few days with
302 clear skies and cold temperatures. From mid February and onward, several low pressure systems
303 passed Scandinavia and Finland, causing high variations in wind speed and direction. From 24
304 February on, the Bothnian Bay was again under the influence of high pressure, creating favorable
305 conditions for SBL development. Relatively, the temperature was mostly mild, with only few
306 days below -10°C . Consistent with the mild weather, the sea ice extent of the Baltic sea in
307 February 2017 was considerably smaller than usual (compared to a reference period of 2006-2018,
308 not shown). The sea ice concentration in the Bothnian Bay grew rapidly from 5-12 February
309 (Figure 4b, c) during the relatively cold period associated with the high pressure system in the
310 beginning of the campaign. From mid February, the large-scale flow packed the ice towards the
311 northeast of the Bothnian Bay, resulting in a local minimum in the sea ice concentration on 18
312 February (Figure 4d). Afterwards, the sea ice concentration gradually increased until the end of
313 the month (Figure 4e).

314 In contrast to the varying synoptic conditions the year before, the weather during ISOBAR18
315 was dominated by high pressure (Figure 4f). In February 2018, temperatures were low, winds were
316 relatively weak and mostly from the north and there were many days with clear skies. An exception
317 to these meteorological conditions occurred during the passage of a low pressure system from the
318 North Sea toward northern Sweden and Finland around 8-16 February, resulting in strong southerly

319 winds and temperatures up to 0 °C. Before and after this period, daily mean temperatures were
320 typically below –10 °C and the wind speed was mostly low to moderate. The high pressure blocking
321 situation during ISOBAR18 is consistent with a colder sea ice season compared to ISOBAR17, with
322 gradually increasing sea ice concentration and thickness during the cold periods of 1-8 February
323 (Figure 4g, h) and 15-23 February (Figure 4i, j). The Bothnian Bay was more or less ice covered
324 throughout the ISOBAR18 campaign.

325 Overall, the sea ice conditions and weather situation were more favorable for the formation
326 of VSBL during ISOBAR18. An overview of the large-scale and corresponding boundary-layer
327 conditions during the 14 IOPs is provided in Table 5.

328 **Synthesis of UAS and ground-based in-situ and remote sensing observations**

329 The two ISOBAR field campaigns comprised a variety of observation systems, thus the synthesis
330 of observations on the basic meteorological parameters, such as wind speed, direction, temperature
331 and humidity, required carefully designed post-processing procedures. In particular the UAS
332 data underwent procedures for sensor calibration, reprocessing of altitude data based on observed
333 pressure and air temperature instead of assuming a standard atmosphere lapse rate, response time
334 correction (UAS thermodynamic parameters) and QA/QC procedures, especially for the wind
335 estimation algorithms. Excellent examples for the quality of this synthesis are the profiles from
336 1510 to 1530 UTC 20 February 2018 when all four profiling UAS (SUMO, B2M, CS2 and Q13)
337 were operated quasi-simultaneously together with the ground-based observations from GFI2, FMI,
338 MFAS and WCv1. The resulting profiles in Figure 5, reveal a very good agreement between the
339 different systems. All UASs and the 10-m mast sample a well-mixed layer up to ~ 100m topped by
340 a sharp inversion. The observed wind speed profiles also agree very well with light winds below
341 2 m s^{-1} in the lowermost 60 m and increasing wind speeds up to 4 m s^{-1} to 5 m s^{-1} , peaking at about

342 200 m. CopterSonde, lidar (WCv1) and sodar (MFAS) show slightly higher wind speeds at this
343 level with the CopterSonde indicating this being related to a LLJ. The SUMO did not reproduce
344 the same peak wind speed at this level, as its wind estimation algorithm (Mayer et al. 2012a)
345 takes data over one full circular flight track into account, which results in a smoother wind profile.
346 Furthermore, the presented wind speed profiles from MFAS and WCv1 represent 30-min averages,
347 whereas UAS profiles are based on quasi-instantaneous observations.

348 **Science highlights**

349 *SBL evolution*

350 During IOP-14, 1615 to 2030 UTC 23 February 2018, UAS based atmospheric profiling with
351 high temporal resolution gives detailed insight into the temporal evolution of the SBL at a spatial
352 resolution on the order of 1 m. This allows for the direct capture of a considerable portion of the
353 turbulent fluctuations, in particular at higher levels, as the size of turbulent eddies is expected to
354 increase with height. Hailuoto was located at the south-eastern flank close to the centre of the
355 high pressure system and under the influence of weak northeasterly flow (Table 5). Clear-sky
356 conditions favored the development of an SBL, transitioning between the weakly stable and very
357 stable regime. Temperature profiles from the three UAS operated during this IOP, i.e., SUMO,
358 B2M and Q13, indicate an overall cooling of the ABL associated with strengthening of the surface-
359 based inversion and increase in inversion depth (Figure 6a). The corresponding near-surface
360 temperature observations (Figure 6b) confirm the trend of surface cooling and intensification of
361 the inversion, which is initiated by long-wave radiative cooling after sunset. Various UAS profiles
362 indicate remarkable, fine-scale structures of thermal instabilities in layers between the surface
363 and approximately 70 m. In particular, the profiles at 1718, 1741 and 1819 UTC consistently

resemble these features. At the same time, we observe a series of rapid temperature changes, most pronounced at the 0.6-m and 2.0-m levels. During the cold episodes, the near-surface wind directions change from about 60° to 10° and exhibit a signature of wind veer resembling an Ekman spiral (Figure 6b). The observed shift in wind direction occurs, however, on time scales much shorter than expected from pure Ekman adjustment, indicating the importance of local advective processes. With the geostrophic wind shifting gradually from roughly 60° to 100° , this results in a surface angle of at least 50° . Note that NWP models in GABLS1 show roughly a surface angle of 30° (Svensson and Holtslag 2009), while theory of Nieuwstadt (1985) predicts 60° . The period from about 1815 until 2000 UTC is characterized by a strong surface inversion and meandering of the flow can be observed at all levels up to 46 m. The second weather station on the sea ice (GFI-1, not shown) recorded a very similar temperature and wind signal, however, the changes occur a couple of minutes earlier and the cold periods last longer. Based on these observations, we conclude that these events are related to the passage of microfronts (i.e., the advection of airmasses with different properties). The measured wind direction suggests the warmer airmass being modified by the presence of land, whereas the colder air originates from a rather clean sea-ice fetch. The observed fine-scale instabilities in the vertical profiles lead us to the hypothesis that these microfronts are rather irregular in their shape, potentially triggered by directional shear.

Disentangling the complexity of the SBL

During IOP-10, 18-19 February 2018, ground-based in-situ and remote sensing systems alongside UAS captured a variety of SBL phenomena during two major periods with very stable stratification, the first of which was from 1330 to 1615 UTC while the second was from about 1930 to 0040 UTC. The large-scale situation was characterized by a high pressure system forming in the Barents Sea and associated weak pressure gradients at its southeastern flank, but varying cloud cover (Table 5).

387 The start of these periods correspond well with strongly negative net-radiation (indicated as colored
388 shading at the top of Figure 7a), due to clear sky conditions. The temperatures observed at GFI2
389 (10-m mast on the sea ice) and FMI (permanent 46-m tower) reveal strong vertical gradients
390 during the VSBL cases and are subject to rapid variations, especially at the 4.5-m and 6.9-m
391 levels. The LATAN-3M sodar echogram indicates a surface-based turbulent layer extending to
392 a maximum altitude of roughly 100 m, but frequently as shallow as 20 m (or even lower) and
393 with occasional elevated turbulent layers above (Figure 7c). The wind profile above the ABL is
394 fairly constant with a weak flow from east-northeast (wind barbs in Figure 7d). Within the ABL,
395 the wind profile is, however, influenced by a variety of processes (e.g., LLJ or submeso motions)
396 resulting in strong variability in both wind direction and magnitude (Figure 7b). In general, IOP-10
397 was characterized by near-calm conditions, with 31 % (63 %) of the 10 min averaged 2-m wind
398 speed below 0.5 ms^{-1} (1.0 ms^{-1}), which makes the SBL susceptible to sporadic mixing events
399 generated by wave-like and other submeso motions (Mahrt 2011). In the following paragraphs
400 we will highlight some of the observations during the subintervals I–III. The complexity of these
401 cases (i.e., non-linear interactions between a variety of different scales, including turbulent and
402 non-turbulent motions) is likely to cause severe problems not only in state-of-the-art NWP but also
403 in other atmospheric research models (e.g., Fernando and Weil 2010; Sun et al. 2015).

404 IOP-10/I, INTENSIFICATION AND COLLAPSE OF THE LLJ

405 The first VSBL-interval is initiated by a rapid temperature drop close to the surface of 2 K within
406 20 s to 30 s (Figure 8a), accompanied by a reduction in wind speed (Figure 8b) and a wind direction
407 shift of 180° from north to south (Figure 8c). During the following minutes (until ca. 1400 UTC)
408 the near-surface winds almost completely calm down, thus increasing the dynamic stability, while
409 the flow at elevated layers around 100 m slightly accelerates and forms a weak LLJ. All three EC

410 systems of GFI2 show weak intermittent turbulence during this period (see w' in Figure 8d and
411 $\overline{w'T'}$ in Figure 8e). Nevertheless, the lowest layers remain at a rather constant temperature; the
412 reason for this is not quite clear. Our mast observations, however, show small-scale oscillations in
413 wind speed and direction at the three lowest levels, which seem rather independent of each other.
414 Occasionally, the local wind and directional shear might be large enough to trigger small-scale
415 mixing events.

416 At about 1535 UTC, the 10-m wind speed accelerates to about 2 ms^{-1} triggering a strong
417 intermittent event, which also influences the two EC levels below, although to a weaker extent.
418 Investigating the evolution of the vertical wind profile (Figure 8g) based on WCv1 lidar and 10-m
419 mast data, suggests that the acceleration of the 10-m wind is related to an increase in wind shear
420 due to the intensification and lowering of the LLJ; eventually this causes a shear instability. The
421 sodar echogram (Figure 7c) supports this interpretation, as it indicates an elevated weak turbulent
422 layer merging with lower levels around 1440 UTC, followed by an increase in turbulence below
423 80 m and the lowering of the elevated inversion layer (Figure 8f). After this event, the wind speed
424 profiles take a more logarithmic shape again. The vertical temperature profiles in Figure 8f also
425 feature a shift from a very shallow and strong surface-based and an additional elevated inversion to
426 a more logarithmic profile after this event. A reduction in radiative cooling due to increased cloud
427 cover initiates the end of this VSBL-period.

428 IOP-10/II, NEAR-SURFACE WAVE INSTABILITY

429 During IOP-10 the instrumentation on the 10-m mast recorded a series of amplifying temperature
430 oscillations, most pronounced at 4.5 m, 6.9 m and 10.3 m (Figure 9a). At 2234 UTC this oscillation
431 results in an remarkable cooling of the 10.3-m temperature, dropping by 4 K within approximately
432 1 min. Associated with this main cooling event is a temporary shift to neutral static stability

433 and enhanced near surface turbulence (Figure 9b). The near-surface stability before this event
434 was characterized by a sharp temperature gradient, $\Delta T_{10\text{m}-0.6\text{m}} \approx 4.5\text{ K}$ and weak winds at about
435 1 ms^{-1} , meandering between south-southwest and north-northeast (Figure 9a). The three sonic
436 anemometers of GFI2 sampled very weak to intermittent turbulence (Figure 9b), whereas the
437 remote sensing systems (e.g., 45-m and 85-m lidar levels in Figure 9b) indicate some wave activity
438 aloft (see also Figure 7b). The signature of this wave can also be detected in the 10-m vertical
439 velocity data.

440 From 2232 UTC the wind at the lowermost levels shifts to a northerly direction, whereas at
441 10 m it stays south-southeast for two more minutes. This results in enhanced local shear as shown
442 in Figure 9c, while the bulk shear is still fairly weak. At the same time, the amplitude of the
443 wave starts to grow rapidly, causing an upward transport of cold, near-surface air at the wave crest
444 at 2233 UTC. This is also associated with a shift to near-neutral stratification as reflected in the
445 substantial drop in the gradient Richardson number (Figure 9d). During the next wave trough, the
446 static stability becomes stable again but the directional shear remains. The following wave crest
447 results in the aforementioned strong elevated cooling event, contributing to further destabilisation
448 of the surface layer (Figure 9d) and the breaking of the wave at 2234 UTC. This wave instability
449 causes enhanced turbulence and a uniform northerly wind direction at all observation levels of the
450 10-m mast. Also the gradient and bulk Richardson numbers drop to values between 0 and 0.25.
451 The following period is characterized by weak but increasing stability with continuous turbulence.
452 Some weaker wave activity remains clearly visible in our observations.

453 Although the origin of the process leading to the shift in wind direction near the surface and
454 the resulting enhanced directional wind shear remains unclear, this case nicely illustrates the
455 importance of local wind shear for triggering the instability of near-surface wave.

457 The LATAN-3M sodar recorded a very clear and strong harmonic signal starting at 0010 UTC
458 (Figure 10f) between 100 m and 200 m, which resulted in a major instability at 0037 UTC. Near the
459 surface, the turbulence was enhanced substantially, as observed by the EC systems at 2.0 m, 4.5 m
460 and 10.3 m (Figure 10d, e). The harmonic oscillations with a period of about 4 min can also be
461 observed in the horizontal and vertical velocity components (Figure 10b and d) of the WCv1 and
462 the 10-m mast. The oscillations in horizontal and vertical velocity are 180° out of phase, consistent
463 with internal gravity waves (Sun et al. 2015).

464 The preceding period is at first characterized by a strong, surface-based inversion (Figure 10a)
465 topping out at about 100 m with light, meandering winds roughly from southeast (Figure 10b and
466 c), occasionally showing the signature of wind veer resembling an Ekman spiral (e.g., as seen
467 around 2310 UTC). The turbulence detected by the three sonic anemometers is very weak and of
468 intermittent character. Between 2340 and 2350 UTC the wind direction shifts to a rather northerly
469 direction at all levels below 200 m (see also Figure 7d) and the wind speeds drop. The upper level
470 winds, at heights between 46 m and 85 m, accelerate gently until the wave breaks at 0037 UTC.

471 For an in-depth analysis, the UAS temperature and lidar wind speed profiles sampled at 2342,
472 0009 and 0030 UTC (mean UAS flight time) offer further insight in the dynamics of this event
473 (Figure 11a). These profiles indicate some cooling above 50 m, whereas wind speeds increase
474 below 75 m and decrease above this level, resulting in the formation of a LLJ as seen in the last
475 profile. This corresponds to strong downward transport of momentum as seen in the time height
476 diagram for wind speed (Figure 11c). Estimates of Ri for the three profiles (Figure 11b) indicate
477 the formation of a dynamically weakly stable layer ($Ri < 0.25$) right below 150 m, between the
478 time of the first and second profile, which then propagates downwards. This locally weakly stable

479 layer is largely related to the sharp wind speed gradients above the LLJ core. Just about 7 min after
480 the last UAS profile, the wave breaks and strongly enhances the turbulence near the surface. The
481 wavelet spectral energy estimate of the vertical wind component observed at 10 m (Figure 11d)
482 indicates very weak turbulence before 0037 UTC. The wave-breaking event is characterized by a
483 very strong signal with a period of about 3 min, which triggers a turbulence cascade to smaller
484 scales. After 0100 UTC, the strong 3 min signal begins to vanish and the small-scale turbulence
485 weakens again.

486 The wave breaking event ends at 0050 UTC and after this the wave appears to have higher
487 frequency (Figure 10f). This is most likely due to the Doppler shift caused by the increasing wind
488 speeds at the levels above 125 m (Figure 11c).

489 **Summary and outlook**

490 ISOBAR is an experimental research project targeting the SBL over Arctic sea ice by means
491 of a novel observational approach based on a combination of ground-based in-situ and remote
492 sensing instrumentation with multiple unmanned aircraft systems. Two major field campaigns,
493 ISOBAR17 and ISOBAR18, were carried out at the Finnish island Hailuoto in the ice-covered
494 Bothnian Bay, each lasting for about one month in February 2017 and 2018. These campaigns were
495 characterized by contrasting conditions, with little sea ice and relatively mild temperatures in 2017,
496 whereas conditions were closer to the climatological mean in 2018, favoring more frequent VSBL
497 formation. With our observation strategy of extensive UAS-based measurements supplemented
498 by surface-based mast and remote sensing observations, we have sampled comprehensive SBL
499 datasets, including 14 IOPs; these datasets offer unprecedented spatiotemporal resolution, while
500 also displaying good agreement between the different systems.

501 Frequent UAS profiles allow for detailed insight into the evolution of the SBL, which may be
502 subject to rapid temperature changes affecting the entire ABL, and small-scale thermal instabilities
503 within the otherwise stably stratified ABL. These data also allow for detailed studies on various
504 VSBL processes and their interaction with near-surface turbulence, of which we highlight three
505 examples, all observed during the same IOP: first, a shear instability caused by the lowering and
506 intensification of the LLJ; second, an unusual rapid-cooling event at elevated levels around 10 m,
507 which appears to be caused by the interaction of a near-surface wave with local shear and the
508 modulation of the surface layer static stability associated with this non-linear wave; third, a wave
509 instability related to the intensification of shear at the top of a forming LLJ, triggering enhanced
510 turbulence near the surface. The nature and interactions of such VSBL processes, as well as the
511 potential deviations from similarity theory associated with them, will be subject to more systematic
512 studies also making use of other SBL datasets such as SHEBA (Grachev et al. 2008) or CASES-99
513 (Poulos et al. 2002).

514 Furthermore, the ISOBAR datasets provide an excellent opportunity to study the transition from
515 WSBL to VSBL, which is important for a better understanding of the conditions leading to strong
516 surface-based temperature inversions and associated extremely cold temperatures. In particular, we
517 aim to investigate the relative importance of local and large-scale conditions. In a follow-up project,
518 we aim to identify and classify the various mechanisms behind the generation of intermittency in
519 the VSBL, based on the ISOBAR and other data sets. This classification should form the basis for a
520 stochastic parameterization for intermittent turbulence in meso-scale NWP models. Additionally,
521 the UAS profiles gathered during ISOBAR — with such unique spatiotemporal resolution — offer a
522 new perspective for SBL studies by applying an alternative gradient-based scaling scheme (Sorbjan
523 2010). The application of this method allows the determination of vertical profiles of turbulent
524 parameters, which could aid the development of new NWP parameterizations.

525 Initial numerical modelling experiments have confirmed that the structure of the VSBL is inade-
526 quately represented in state-of-the-art NWP and SCM. A complementary LES experiment showed
527 that turbulence-resolving simulations are able to reproduce even very shallow stable layers and
528 thus provide a powerful tool for studying turbulent processes in such conditions. In a next step we
529 thus plan to perform an LES study to evaluate the gradient-based similarity relationships. In this
530 way, we hope to develop a turbulence parameterization, to be implemented in both NWP and SCM
531 models and finally to be evaluated against measurement data obtained during the IOP periods.
532 Moreover, we strive to analyze LES data with respect to phenomena observed during the IOPs and
533 to perform virtual flights in the LES model to evaluate and improve flight strategies for future UAS
534 campaigns.

535 **Sidebar: SBL model simulations**

536 To illustrate current challenges in SBL modelling, three different types of numerical models
537 were used to simulate the SBL evolution during IOP-14 (23-24 February 2018): the MetCoOp
538 Ensemble Prediction System (MEPS), the Weather Research and Forecasting model in its single-
539 column mode (WRF-SCM), and the large-eddy simulation (LES) model PALM. MEPS (Müller
540 et al. 2017) is an operational NWP system covering the Nordic countries, forced at its boundaries
541 by the global ECMWF-IFS (Bauer et al. 2013). There are 65 vertical model levels, with the first
542 level at 12.5 magl and decreasing vertical resolution aloft. Surface-atmosphere and surface-soil
543 processes are described by the SURFEX model (Masson et al. 2013). WRF-SCM utilizes the
544 full WRF physics (Skamarock et al. 2008), with Mellor–Yamada–Nakanishi–Niino turbulence
545 parameterization (Nakanishi and Niino 2006), within an atmospheric column with 200 vertical
546 levels. The vertical spacing is about 2 m in the lower atmosphere. Hourly geostrophic winds and
547 advection of momentum, temperature and humidity are derived from a meso-scale WRF simulation

548 (Sterk et al. 2015). PALM (Maronga et al. 2015, 2020) runs at a grid spacing of 2 m and a model
549 domain of 500^3 m^3 using a standard configuration but with a modified Deardorff subgrid-scale
550 closure as described by Dai et al. (2020) and coupled to the Rapid Radiative Transfer Model
551 (Clough et al. 2005). PALM is initialized by the same vertical profiles as WRF-SCM and forced
552 by skin temperatures observed during IOP-14.

553 Figure 12 shows that even though all three models are capable of forming a very stable strati-
554 fication and cold air at the surface, the model results differ considerably. The formation of cold
555 air above the surface and the associated strong vertical (temperature) gradients are best captured
556 by PALM, while both MEPS and WRF-SCM display a deeper SBL with weaker gradients. At
557 heights between 50 m and 300 m, both WRF-SCM and PALM produce weaker temperature gra-
558 dients, which can be ascribed to deficiencies in the model initialization. MEPS here captures the
559 stratification much better. Overall, the three different models show substantial deviations from the
560 observations in the lower atmosphere.

561 Likely sources for these deviations are the turbulence parameterizations which overestimate
562 turbulent mixing and the associated downward heat flux from the atmosphere to the cold surface,
563 and the different boundary conditions and initial conditions applied. As PALM resolves most of
564 the turbulent transport, it can more adequately represent the SBL evolution close to the surface. It
565 is noteworthy that PALM and WRF-SCM, despite being initialized with the same profiles, produce
566 quite different SBLs. Research models like WRF-SCM and PALM are highly sensitive to the
567 initial profiles and boundary conditions, which are either derived from measurements or larger-
568 scale model data and thus come with an inherent uncertainty. All three models depend on accurate
569 surface properties, for which a combination of measurements and ad-hoc estimations was used
570 here. The differences present in these simulations epitomise the necessity for deeper understanding
571 of the SBL and its representation in atmospheric models; an understanding which is expedited

572 by unique, fine-scale observational datasets, such as ISOBAR. Sensitivities to model physics and
573 surface properties during IOP-14 are subject of an ongoing study, following the process-based
574 analysis by Sterk et al. (2016).

575 *Acknowledgments.* We would like to acknowledge all campaign participants (see Table 1) for their
576 dedication and enthusiasm that largely contributed to the success of the two field campaigns in
577 often challenging conditions. A special thanks from all participants is dedicated to our local hosts
578 at Hailuodon Majakkapiha, Hannu Korpela, Sanna Ahomäki and Pekka Tervonen. Hannu and
579 Sanna were just amazing in perfectly organizing all required logistics and solving all the large and
580 small challenges and problems certainly occurring during extensive field work. And our campaign
581 chef Pekka was spoiling us with superb meals, an important factor for a successful campaign
582 that never should be underestimated. Furthermore, we would like to thank Anak Bhandari for
583 his efforts and commitment in the preparation of the instrumentation upfront the campaign, the
584 organization of the transport and the clean-up after return. We would also like to thank Priit
585 Tisler from FMI for his advice on UAS operations in Finland and for connecting us with the right
586 persons and organizations. With respect to the flight permission process we are very grateful to the
587 Finnish aviation authority TRAFI for their very positive attitude, competent guidance and a fast
588 and non-bureaucratic handling of our applications. We also highly appreciate the uncomplicated
589 communication with the Air Traffic Control (ATC) at Oulu airport that allowed us to focus on
590 science when operating UAS.

591 The ISOBAR project was funded by the Research Council of Norway (RCN) under the
592 FRINATEK scheme (project number: 251042/F20). The scanning wind lidar system (WC100S),
593 used during ISOBAR17 and the WCv1 lidar wind profiler and the MFAS sodar used during
594 ISOBAR18, have been made available via the National Norwegian infrastructure project OBLO

595 (Offshore Boundary Layer Observatory) also funded by RCN (project number: 227777). The work
596 of GHU, TV and IS was also supported by the Academy of Finland (contract 304345). Financial
597 support was also provided in part by the National Science Foundation under Grant No. 1539070 and
598 internal funding from the University of Oklahoma. The WRF-SCM simulations were performed
599 on resources provided by UNINETT Sigma2 - the National Infrastructure for High Performance
600 Computing and Data Storage in Norway. Finally we would like to express our gratitude to our
601 esteemed colleague Zbigniew Sorbjan, who unfortunately passed away by far too early in February
602 2017, just during the first ISOBAR campaign.

603 APPENDIX

604 List of Abbreviations

605 References

- 606 Atlaskin, E., and T. Vihma, 2012: Evaluation of NWP results for wintertime nocturnal boundary-
607 layer temperatures over Europe and Finland. *Quart. J. Roy. Meteor. Soc.*, **138 (667)**, 1440–1451,
608 doi:10.1002/qj.1885.
- 609 Bauer, P., and Coauthors, 2013: *Model Cycle 38r2: Components and Performance*. European
610 Centre for Medium-Range Weather Forecasts.
- 611 Beare, R. J., 2007: Boundary layer mechanisms in extratropical cyclones. *Quart. J. Roy. Meteor.*
612 *Soc.*, **133 (623)**, 503–515, doi:10.1002/qj.30.
- 613 Bell, T. M., B. R. Greene, P. M. Klein, M. Carney, and P. B. Chilson, 2020: Confronting the
614 boundary layer data gap: evaluating new and existing methodologies of probing the lower
615 atmosphere. *Atmos. Meas. Tech.*, **13 (7)**, 3855–3872, doi:10.5194/amt-13-3855-2020.

- 616 Bintanja, R., E. C. van der Linden, and W. Hazeleger, 2012: Boundary layer stability and Arctic
617 climate change: A feedback study using EC-Earth. *Climate Dyn.*, **39** (11), 2659–2673, doi:
618 10.1007/s00382-011-1272-1.
- 619 Bonin, T., P. Chilson, B. Zielke, and E. Fedorovich, 2013: Observations of the early evening
620 boundary-layer transition using a small unmanned aerial system. *Bound.-Layer Meteor.*, **146** (1),
621 119–132, doi:10.1007/s10546-012-9760-3.
- 622 Bosveld, F. C., and Coauthors, 2014: The third GABLS intercomparison case for evaluation studies
623 of boundary-layer models. Part B: Results and process understanding. *Bound.-Layer Meteor.*,
624 **152** (2), 157–187, doi:10.1007/s10546-014-9919-1.
- 625 Byrkjedal, Ø., I. Esau, and N. G. Kvamstø, 2007: Sensitivity of simulated wintertime Arctic
626 atmosphere to vertical resolution in the ARPEGE/IFS model. *Climate Dyn.*, **30** (7-8), 687–701,
627 doi:10.1007/s00382-007-0316-z.
- 628 Cassano, J. J., 2013: Observations of atmospheric boundary layer temperature profiles with a small
629 unmanned aerial vehicle. *Antarct. Sci.*, **26** (02), 205–213.
- 630 Cassano, J. J., J. A. Maslanik, C. J. Zappa, A. L. Gordon, R. I. Cullather, and S. L. Knuth, 2010:
631 Observations of Antarctic polynya with unmanned aircraft systems. *EOS, Trans., Amer. Geophys.*
632 *Union*, **91** (28), 245, doi:10.1029/2010eo280001.
- 633 Chilson, P. B., and Coauthors, 2009: SMARTSonde: A small UAS platform to support radar
634 research. *Proceedings of the 34th Conference on Radar Meteorology*, URL http://ams.confex.com/ams/34Radar/techprogram/paper_156396.htm.
635
- 636 Clough, S. A., M. W. Shephard, E. J. Mlawer, J. S. Delamere, M. J. Iacono, K. Cady-Pereira,
637 S. Boukabara, and P. D. Brown, 2005: Atmospheric radiative transfer modeling: A summary

638 of the AER codes. *J. Quant. Spectrosc. Radiat. Transfer*, **91** (2), 233–244, doi:10.1016/j.jqsrt.
639 2004.05.058.

640 Curry, J. A., J. Maslanik, G. Holland, and J. Pinto, 2004: Applications of aerosondes in the arctic.
641 *Bull. Amer. Meteor. Soc.*, **85** (12), 1855–1862, doi:10.1175/bams-85-12-1855.

642 Cuxart, J., and Coauthors, 2000: Stable atmospheric boundary-layer experiment in Spain (SABLES
643 98): A report. *Bound.-Layer Meteor.*, **96** (3), 337–370, doi:10.1023/a:1002609509707.

644 Cuxart, J., and Coauthors, 2005: Single-column model intercomparison for a stably strat-
645 ified atmospheric boundary layer. *Bound.-Layer Meteor.*, **118** (2), 273–303, doi:10.1007/
646 s10546-005-3780-1.

647 Cuxart, J., and Coauthors, 2016: Estimation of the advection effects induced by surface het-
648 erogeneities in the surface energy budget. *Atmos. Chem. Phys.*, **16** (14), 9489–9504, doi:
649 10.5194/acp-16-9489-2016.

650 Dai, A., D. Luo, M. Song, and J. Liu, 2019: Arctic amplification is caused by sea-ice loss under
651 increasing CO₂. *Nat. Commun.*, **10** (1), doi:10.1038/s41467-018-07954-9.

652 Dai, Y., S. Basu, B. Maronga, and S. R. de Roode, 2020: Addressing the grid-size sensitivity
653 issue in large-eddy simulations of stable boundary layers. *Bound.-Layer Meteor.*, in review,
654 2003.09463v1.

655 Davy, R., and I. Esau, 2016: Differences in the efficacy of climate forcings explained by variations
656 in atmospheric boundary layer depth. *Nat. Commun.*, **7** (1), 11 690, doi:10.1038/ncomms11690.

657 de Boer, G., and Coauthors, 2015: The Pilatus unmanned aircraft system for lower atmospheric
658 research. *Atmos. Meas. Tech.*, **9**, 1845–1857, doi:10.5194/amtd-8-11987-2015.

659 de Boer, G., and Coauthors, 2018: A bird's-eye view: Development of an operational
660 ARM unmanned aerial capability for atmospheric research in Arctic Alaska. *Bull. Amer.*
661 *Meteor. Soc.*, **99** (6), 1197–1212, doi:10.1175/BAMS-D-17-0156.1, [https://doi.org/10.1175/
662 BAMS-D-17-0156.1](https://doi.org/10.1175/BAMS-D-17-0156.1).

663 de Boer, G., and Coauthors, 2019: Development of community, capabilities and understanding
664 through unmanned aircraft-based atmospheric research: The LAPSE-RATE campaign. *Bull.*
665 *Amer. Meteor. Soc.*, doi:10.1175/bams-d-19-0050.1.

666 de Wiel, B. J. H. V., and Coauthors, 2017: Regime transitions in near-surface temperature inver-
667 sions: A conceptual model. *J. Atmos. Sci.*, **74** (4), 1057–1073, doi:10.1175/jas-d-16-0180.1.

668 Egger, J., and Coauthors, 2002: Diurnal winds in the Himalayan Kali Gandaki Valley. Part
669 III: Remotely piloted aircraft soundings. *Mon. Wea. Rev.*, **130** (8), 2042–2058, doi:10.1175/
670 1520-0493(2002)130<2042:DWITHK>2.0.CO;2.

671 Egger, J., and Coauthors, 2005: Diurnal circulation of the Bolivian altiplano. Part I: Observations.
672 *Mon. Wea. Rev.*, **133** (4), 911–924, doi:10.1175/MWR2894.1.

673 Elston, J., B. Argrow, M. Stachura, D. Weibel, D. Lawrence, and D. Pope, 2015: Overview of
674 small fixed-wing unmanned aircraft for meteorological sampling. *J. Atmos. Oceanic Technol.*,
675 **32** (1), 97–115, doi:10.1175/JTECH-D-13-00236.1.

676 Fernando, H. J. S., and J. C. Weil, 2010: Whither the stable boundary layer? *Bull. Amer.*
677 *Meteor. Soc.*, **91** (11), 1475–1484, doi:10.1175/2010BAMS2770.1, [https://doi.org/10.1175/
678 2010BAMS2770.1](https://doi.org/10.1175/2010BAMS2770.1).

679 Fernando, H. J. S., and Coauthors, 2015: The MATERHORN: Unraveling the intricacies of moun-
680 tain weather. *Bull. Amer. Meteor. Soc.*, **96** (11), 1945–1967, doi:10.1175/BAMS-D-13-00131.1.

- 681 Foken, T., 2006: 50 years of the Monin–Obukhov similarity theory. *Bound.-Layer Meteor.*, **119**,
682 431–447, doi:10.1007/s10546-006-9048-6.
- 683 Gentine, P., G.-J. Steeneveld, B. G. Heusinkveld, and A. A. Holtslag, 2018: Coupling between
684 radiative flux divergence and turbulence near the surface. *Quart. J. Roy. Meteor. Soc.*, **144 (717)**,
685 2491–2507, doi:10.1002/qj.3333.
- 686 Goger, B., M. W. Rotach, A. Gohm, O. Fuhrer, I. Stiperski, and A. A. M. Holtslag, 2018: The
687 impact of three-dimensional effects on the simulation of turbulence kinetic energy in a major
688 Alpine valley. *Bound.-Layer Meteor.*, **168 (1)**, 1–27, doi:10.1007/s10546-018-0341-y.
- 689 Grachev, A. A., E. L. Andreas, C. W. Fairall, P. S. Guest, and P. O. G. Persson, 2008: Turbulent
690 measurements in the stable atmospheric boundary layer during SHEBA: Ten years after. *Acta*
691 *Geophys.*, **56 (1)**, 142–166, doi:10.2478/s11600-007-0048-9.
- 692 Grachev, A. A., E. L. Andreas, C. W. Fairall, P. S. Guest, and P. O. G. Persson, 2013: The critical
693 richardson number and limits of applicability of local similarity theory in the stable boundary
694 layer. *Bound.-Layer Meteor.*, **147 (1)**, 51–82, doi:10.1007/s10546-012-9771-0.
- 695 Graham, R. M., and Coauthors, 2019: Evaluation of six atmospheric reanalyses over Arctic sea ice
696 from winter to early summer. *J. Climate*, **32 (14)**, 4121–4143, doi:10.1175/jcli-d-18-0643.1.
- 697 Greene, B., A. Segales, T. Bell, E. Pillar-Little, and P. Chilson, 2019: Environmental and sensor
698 integration influences on temperature measurements by rotary-wing unmanned aircraft systems.
699 *Sensors*, **19 (6)**, 1470, doi:10.3390/s19061470.
- 700 Heppelmann, T., A. Steiner, and S. Vogt, 2017: Application of numerical weather prediction
701 in wind power forecasting: Assessment of the diurnal cycle. *Meteorol. Z.*, **26 (3)**, 319–331,
702 doi:10.1127/metz/2017/0820.

- 703 Hersbach, H., and Coauthors, 2020: The ERA5 global reanalysis. *Quart. J. Roy. Meteor. Soc.*,
704 doi:10.1002/qj.3803.
- 705 Hoch, S. W., P. Calanca, R. Philipona, and A. Ohmura, 2007: Year-round observation of longwave
706 radiative flux divergence in Greenland. *J. Appl. Meteor. Climatol.*, **46** (9), 1469–1479, doi:
707 10.1175/JAM2542.1.
- 708 Holland, G. J., and Coauthors, 2001: The Aerosonde Robotic Aircraft: A new paradigm for environ-
709 mental observations. *Bull. Amer. Meteor. Soc.*, **82** (5), 889–901, doi:10.1175/1520-0477(2001)
710 082<0889:TARAAN>2.3.CO;2.
- 711 Holtslag, A., and Coauthors, 2013: Stable atmospheric boundary layers and diurnal cycles –
712 challenges for weather and climate models. *Bull. Amer. Meteor. Soc.*, **94** (11), 1691–1706,
713 doi:10.1175/BAMS-D-11-00187.1.
- 714 Houston, A. L., B. Argrow, J. Elston, J. Lahowetz, E. W. Frew, and P. C. Kennedy, 2012: The
715 collaborative Colorado–Nebraska unmanned aircraft system experiment. *Bull. Amer. Meteor.*
716 *Soc.*, **93** (1), 39–54, doi:10.1175/2011bams3073.1.
- 717 Jakobson, E., T. Vihma, T. Palo, L. Jakobson, H. Keernik, and J. Jaagus, 2012: Validation of
718 atmospheric reanalyses over the central Arctic Ocean. *Geophys. Res. Lett.*, **39** (10), n/a–n/a,
719 doi:10.1029/2012gl051591.
- 720 Jonassen, M., P. Tisler, B. Altstädter, A. Scholtz, T. Vihma, A. Lampert, G. König-Langlo, and
721 C. Lüpkes, 2015: Application of remotely piloted aircraft systems in observing the atmospheric
722 boundary layer over Antarctic sea ice in winter. *Polar Res.*, **34** (0), doi:10.3402/polar.v34.25651.

- 723 Jonassen, M. O., H. Ólafsson, H. Ágústsson, O. Rögnvaldsson, and J. Reuder, 2012: Improving
724 high-resolution numerical weather simulations by assimilating data from an unmanned aerial
725 system. *Mon. Wea. Rev.*, **140** (11), 3734–3756, doi:10.1175/MWR-D-11-00344.1.
- 726 Jonassen, M. O., I. Välisuo, T. Vihma, P. Uotila, A. P. Makshtas, and J. Launiainen, 2019:
727 Assessment of atmospheric reanalyses with independent observations in the Weddell Sea, the
728 Antarctic. *J. Geophys. Res.: Atmos.*, doi:10.1029/2019jd030897.
- 729 Karsisto, V., S. Tijm, and P. Nurmi, 2017: Comparing the performance of two road weather models
730 in the Netherlands. *Wea. Forecasting*, **32** (3), 991–1006, doi:10.1175/WAF-D-16-0158.1.
- 731 Knuth, S. L., and J. J. Cassano, 2014: Estimating sensible and latent heat fluxes using the integral
732 method from in situ aircraft measurements. *J. Atmos. Oceanic Technol.*, **31** (9), 1964–1981,
733 doi:10.1175/JTECH-D-14-00008.1, <http://dx.doi.org/10.1175/JTECH-D-14-00008.1>.
- 734 Konrad, T. G., M. L. Hill, J. R. Rowland, and J. H. Meyer, 1970: A small, radio-controlled aircraft
735 as a platform for meteorological sensor. *APL Technical Digest*, **10**, 11–19, 19710054637.
- 736 Kouznetsov, R. D., 2009: The multi-frequency sodar with high temporal resolution. *Meteorol. Z.*,
737 **18** (2), 169–173, doi:10.1127/0941-2948/2009/0373.
- 738 Kral, S., and Coauthors, 2018: Innovative strategies for observations in the arctic atmospheric
739 boundary layer (ISOBAR)—the Hailuoto 2017 campaign. *Atmosphere*, **9** (7), 268, doi:10.3390/
740 atmos9070268.
- 741 Kumer, V.-M., J. Reuder, M. Dorninger, R. Zauner, and V. Grubišić, 2016: Turbulent kinetic
742 energy estimates from profiling wind LiDAR measurements and their potential for wind energy
743 applications. *Renewable Energy*, **99**, 898–910, doi:10.1016/j.renene.2016.07.014.

- 744 Kumer, V.-M., J. Reuder, and B. R. Furevik, 2014: A comparison of LiDAR and radiosonde wind
745 measurements. *Energy Procedia*, **53**, 214–220, doi:10.1016/j.egypro.2014.07.230.
- 746 Langford, J. S., and K. A. Emanuel, 1993: An unmanned aircraft for dropwindsonde de-
747 ployment and hurricane reconnaissance. *Bull. Amer. Meteor. Soc.*, **74** (3), 367–375, doi:
748 10.1175/1520-0477(1993)074<0367:AUAFFD>2.0.CO;2.
- 749 Lapworth, A., and S. R. Osborne, 2019: Gravity-wave drag in the stable boundary layer over
750 moderate terrain. *Bound.-Layer Meteor.*, **171** (2), 175–189, doi:10.1007/s10546-018-00422-3.
- 751 Lesins, G., T. J. Duck, and J. R. Drummond, 2012: Surface energy balance framework for Arctic
752 amplification of climate change. *J. Climate*, **25** (23), 8277–8288, doi:10.1175/JCLI-D-11-00711.
753 1.
- 754 Lothon, M., and Coauthors, 2014: The BLLAST field experiment: Boundary-layer late af-
755 ternoon and sunset turbulence. *Atmos. Chem. Phys.*, **14** (20), 10931–10960, doi:10.5194/
756 acp-14-10931-2014.
- 757 Louis, J.-F., 1979: A parametric model of vertical eddy fluxes in the atmosphere. *Bound.-Layer*
758 *Meteor.*, **17** (2), 187–202, doi:10.1007/BF00117978.
- 759 Mahrt, L., 2003: BOUNDARY LAYERS | stably stratified boundary layer. *Encyclopedia of*
760 *Atmospheric Sciences*, Elsevier, 298–305, doi:10.1016/b0-12-227090-8/00091-9.
- 761 Mahrt, L., 2011: The near-calm stable boundary layer. *Bound.-Layer Meteor.*, **140** (3), 343–360,
762 doi:10.1007/s10546-011-9616-2.
- 763 Mahrt, L., 2014: Stably stratified atmospheric boundary layers. *Annu. Rev. Fluid Mech.*, **46**, 23–45,
764 doi:10.1146/annurev-fluid-010313-141354.

- 765 Maronga, B., and Coauthors, 2015: The Parallelized Large-Eddy Simulation Model (PALM)
766 version 4.0 for atmospheric and oceanic flows: Model formulation, recent developments, and
767 future perspectives. *Geosci. Model Dev.*, **8** (8), 2515–2551, doi:10.5194/gmd-8-2515-2015.
- 768 Maronga, B., and Coauthors, 2020: Overview of the PALM model system 6.0. *Geosci. Model*
769 *Dev.*, **13**, 1335–1372, doi:10.5194/gmd-13-1335-2020.
- 770 Martínez, D., M. A. Jiménez, J. Cuxart, and L. Mahrt, 2010: Heterogeneous nocturnal cooling
771 in a large basin under very stable conditions. *Bound.-Layer Meteor.*, **137** (1), 97–113, doi:
772 10.1007/s10546-010-9522-z.
- 773 Masson, V., and Coauthors, 2013: The SURFEXv7.2 land and ocean surface platform for coupled
774 or offline simulation of earth surface variables and fluxes. *Geoscientific Model Development*,
775 **6** (4), 929–960, doi:10.5194/gmd-6-929-2013.
- 776 Mayer, S., G. Hattenberger, P. Brisset, M. Jonassen, and J. Reuder, 2012a: A ‘no-flow-sensor’ wind
777 estimation algorithm for unmanned aerial systems. *International Journal of Micro Air Vehicles*,
778 **4** (1), 15–30, doi:10.1260/1756-8293.4.1.15.
- 779 Mayer, S., M. Jonassen, A. Sandvik, and J. Reuder, 2012b: Profiling the Arctic stable boundary
780 layer in Advent Valley, Svalbard: Measurements and simulations. *Bound.-Layer Meteor.*, **143** (3),
781 507–526, doi:10.1007/s10546-012-9709-6.
- 782 Mayer, S., A. Sandvik, M. Jonassen, and J. Reuder, 2012c: Atmospheric profiling with the UAS
783 SUMO: a new perspective for the evaluation of fine-scale atmospheric models. *Meteorol. Atmos.*
784 *Phys.*, **116** (1-2), 15–26, doi:10.1007/s00703-010-0063-2.

- 785 McNider, R. T., J. R. Christy, and A. Biazar, 2010: A stable boundary layer perspective on global
786 temperature trends. *IOP Conference Series: Earth and Environmental Science*, **13 (1)**, 012 003,
787 doi:10.1088/1755-1315/13/1/012003.
- 788 Monin, A. S., and A. M. Obukhov, 1954: Osnovnye zakonomernosti turbulentnogo peremeshivaniya
789 v prizemnom sloe atmosfery (Basic laws of turbulent mixing in the atmosphere near the ground).
790 *TRUDY GEOFIZ. INST. AKAD. NAUK SSSR*, **24 (151)**, 163–187.
- 791 Müller, M., and Coauthors, 2017: AROME-MetCoOp: A Nordic convective-scale operational
792 weather prediction model. *Wea. Forecasting*, **32 (2)**, 609–627.
- 793 Nakanishi, M., and H. Niino, 2006: An improved Mellor–Yamada level-3 model: Its numerical
794 stability and application to a regional prediction of advection fog. *Bound.-Layer Meteor.*, **119 (2)**,
795 397–407, doi:10.1007/s10546-005-9030-8.
- 796 Nappo, C., 2012: *An Introduction to Atmospheric Gravity Waves*. Academic Press, 400 pp.
- 797 Neumann, P. P., and M. Bartholmai, 2015: Real-time wind estimation on a micro unmanned
798 aerial vehicle using its inertial measurement unit. *Sens. Actuators, A*, **235**, 300–310, doi:http:
799 //dx.doi.org/10.1016/j.sna.2015.09.036.
- 800 Nieuwstadt, F. T. M., 1984: The turbulent structure of the stable, nocturnal boundary layer. *J.*
801 *Atmos. Sci.*, **41 (14)**, 2202–2216, doi:10.1175/1520-0469(1984)041<2202:TTSOTS>2.0.CO;2.
- 802 Nieuwstadt, F. T. M., 1985: A model for the stationary, stable boundary layer. *Turbulence and*
803 *diffusion in stable environments.*, J. C. R. Hunt, Ed., Clarendon Press, Oxford, 149–179.
- 804 Palomaki, R. T., N. T. Rose, M. van den Bossche, T. J. Sherman, and S. F. J. D. Wekker, 2017: Wind
805 estimation in the lower atmosphere using multicopter aircraft. *J. Atmos. Oceanic Technol.*, **34 (5)**,
806 1183–1191, doi:10.1175/JTECH-D-16-0177.1, https://doi.org/10.1175/JTECH-D-16-0177.1.

- 807 Persson, P. O. G., C. W. Fairall, E. L. Andreas, P. G. Guest, and D. K. Perovich, 2002: Measurements
808 near the atmospheric surface flux group tower at SHEBA: Near-surface conditions and surface
809 energy budget. *J. Geophys. Res.*, **107** (C10), doi:10.1029/2000jc000705.
- 810 Pithan, F., and T. Mauritsen, 2014: Arctic amplification dominated by temperature feedbacks in
811 contemporary climate models. *Nat. Geosci.*, **7** (3), 181–184, doi:10.1038/ngeo2071.
- 812 Poulos, G. S., and Coauthors, 2002: CASES-99: A comprehensive investigation of the stable noc-
813 turnal boundary layer. *Bull. Amer. Meteor. Soc.*, **83** (4), 555–581, doi:10.1175/1520-0477(2002)
814 083<0555:caciot>2.3.co;2.
- 815 Rautenberg, A., and Coauthors, 2019: The multi-purpose airborne sensor carrier MASC-3 for
816 wind and turbulence measurements in the atmospheric boundary layer. *Sensors*, **19** (10), 2292,
817 doi:10.3390/s19102292.
- 818 Reuder, J., L. Båserud, M. O. Jonassen, S. T. Kral, and M. Müller, 2016: Exploring the potential
819 of the RPA system SUMO for multipurpose boundary-layer missions during the BLLAST
820 campaign. *Atmos. Meas. Tech.*, **9** (6), 2675–2688, doi:10.5194/amt-9-2675-2016.
- 821 Reuder, J., P. Brisset, M. Jonassen, Marius Müller, and S. Mayer, 2009: The Small Unmanned
822 Meteorological Observer SUMO: A new tool for atmospheric boundary layer research. *Meteorol.*
823 *Z.*, **18** (2), 141–147, doi:10.1127/0941-2948/2009/0363.
- 824 Reuder, J., M. O. Jonassen, and H. Ólafsson, 2012a: The Small Unmanned Meteorological Ob-
825 server SUMO: Recent developments and applications of a micro-UAS for atmospheric boundary
826 layer research. *Acta Geophys.*, **60** (5), 1454–1473, doi:10.2478/s11600-012-0042-8.

827 Reuder, J., and Coauthors, 2012b: FLOHOF 2007: An overview of the mesoscale meteorological
828 field campaign at Hofsjökull, Central Iceland. *Meteorol. Atmos. Phys.*, **116 (1-2)**, 1–13, doi:
829 10.1007/s00703-010-0118-4.

830 Román-Cascón, C., C. Yagüe, G.-J. Steeneveld, G. Morales, J. A. Arrillaga, M. Sastre, and
831 G. Maqueda, 2019: Radiation and cloud-base lowering fog events: Observational analysis and
832 evaluation of WRF and HARMONIE. *Atmos. Res.*, **229**, 190–207, doi:10.1016/j.atmosres.2019.
833 06.018.

834 Segales, A. R., B. R. Greene, T. M. Bell, W. Doyle, J. J. Martin, E. A. Pillar-Little, and P. B.
835 Chilson, 2020: The CopterSonde: An insight into the development of a smart unmanned aircraft
836 system for atmospheric boundary layer research. *Atmospheric Measurement Techniques*, **13 (5)**,
837 2833–2848, doi:10.5194/amt-13-2833-2020.

838 Serreze, M. C., A. P. Barrett, J. C. Stroeve, D. N. Kindig, and M. M. Holland, 2009: The emergence
839 of surface-based Arctic amplification. *The Cryosphere*, **3 (1)**, 11–19, doi:10.5194/tc-3-11-2009.

840 Serreze, M. C., and R. G. Barry, 2011: Processes and impacts of Arctic amplification: A research
841 synthesis. *Global Planet. Change*, **77 (1-2)**, 85–96, doi:10.1016/j.gloplacha.2011.03.004.

842 Skamarock, W., J. Klemp, J. Dudhia, D. Gill, D. Barker, M. Duda, X.-Y. Huang, and W. Wang, 2008:
843 A Description of the Advanced Research WRF Version 3. Tech. Rep. NCAR/TN-475+STR,
844 NCAR. doi:10.5065/D68S4MVH, technical note.

845 Sorbjan, Z., 2010: Gradient-based scales and similarity laws in the stable boundary layer. *Quart.*
846 *J. Roy. Meteor. Soc.*, **136 (650)**, 1243–1254, doi:10.1002/qj.638.

847 Sorbjan, Z., and A. Grachev, 2010: An evaluation of the flux–gradient relationship in the stable
848 boundary layer. *Bound.-Layer Meteor.*, **135 (3)**, 385–405, doi:10.1007/s10546-010-9482-3.

- 849 Spiess, T., J. Bange, M. Buschmann, and P. Vörsmann, 2007: First application of the meteorological
850 Mini-UAV 'M2AV'. *Meteorol. Z.*, **16** (2), 159–169, doi:10.1127/0941-2948/2007/0195.
- 851 Steeneveld, G. J., A. A. M. Holtslag, C. J. Nappo, B. J. H. van de Wiel, and L. Mahrt, 2008:
852 Exploring the possible role of small-scale terrain drag on stable boundary layers over land. *J.*
853 *Appl. Meteor. Climate*, **47** (10), 2518–2530, doi:10.1175/2008jamc1816.1.
- 854 Steeneveld, G. J., M. J. J. Wokke, C. D. G. Zwaaftink, S. Pijlman, B. G. Heusinkveld, A. F. G.
855 Jacobs, and A. A. M. Holtslag, 2010: Observations of the radiation divergence in the surface
856 layer and its implication for its parameterization in numerical weather prediction models. *J.*
857 *Geophys. Res.*, **115** (D6), doi:10.1029/2009jd013074.
- 858 Stephens, G. L., and Coauthors, 2000: The Department of Energy's atmospheric radiation measure-
859 ment (ARM) unmanned aerospace vehicle (UAV) program. *Bull. Amer. Meteor. Soc.*, **81** (12),
860 2915–2938, doi:10.1175/1520-0477(2000)081<2915:tdoesa>2.3.co;2.
- 861 Sterk, H. A. M., G. J. Steeneveld, F. C. Bosveld, T. Vihma, P. S. Anderson, and A. A. M. Holtslag,
862 2016: Clear-sky stable boundary layers with low winds over snow-covered surfaces. Part 2:
863 Process sensitivity. *Quart. J. Roy. Meteor. Soc.*, **142** (695), 821–835, doi:10.1002/qj.2684.
- 864 Sterk, H. A. M., G. J. Steeneveld, T. Vihma, P. S. Anderson, F. C. Bosveld, and A. A. M. Holtslag,
865 2015: Clear-sky stable boundary layers with low winds over snow-covered surfaces. Part 1: WRF
866 model evaluation. *Quart. J. Roy. Meteor. Soc.*, **141** (691), 2165–2184, doi:10.1002/qj.2513.
- 867 Sun, J., and Coauthors, 2015: Review of wave–turbulence interactions in the stable atmospheric
868 boundary layer. *Rev. Geophys.*, **53** (3), 956–993, doi:10.1002/2015rg000487.

- 869 Sun, Q. Z., T. Vihma, M. O. Jonassen, and Z. H. Zhang, 2020: Impact of assimilation of radiosonde
870 and UAV-observations from the Southern Ocean in the polar WRF model. *Adv. Atmos. Sci.*, **37**,
871 doi:10.1007/s00376-020-9213-8.
- 872 Svensson, G., and A. A. M. Holtslag, 2009: Analysis of model results for the turning of the
873 wind and related momentum fluxes in the stable boundary layer. *Bound.-Layer Meteor.*, **132** (2),
874 261–277, doi:10.1007/s10546-009-9395-1.
- 875 Tjernström, M., and Coauthors, 2005: Modelling the Arctic boundary layer: An evaluation of
876 six ARCMIP regional-scale models using data from the SHEBA project. *Bound.-Layer Meteor.*,
877 **117** (2), 337–381, doi:10.1007/s10546-004-7954-z.
- 878 Uotila, P., T. Vihma, and J. Haapala, 2015: Atmospheric and oceanic conditions and the extremely
879 low Bothnian Bay sea ice extent in 2014/2015. *Geophys. Res. Lett.*, **42** (18), 7740–7749, doi:
880 10.1002/2015gl064901.
- 881 Uppala, S. M., and Coauthors, 2005: The ERA-40 re-analysis. *Quart. J. Roy. Meteor. Soc.*,
882 **131** (612), 2961–3012, doi:10.1256/qj.04.176.
- 883 Uttal, T., and Coauthors, 2002: Surface heat budget of the Arctic Ocean. *Bull. Amer. Meteor. Soc.*,
884 **83** (2), 255–275, doi:10.1175/1520-0477(2002)083<0255:SHBOTA>2.3.CO;2.
- 885 Wildmann, N., M. Hofsäb, F. Weimer, A. Joos, and J. Bange, 2014: MASC – a small re-
886 motely piloted aircraft (RPA) for wind energy research. *Adv. Sci. Res.*, **11**, 55–61, doi:
887 10.5194/asr-11-55-2014.
- 888 Wrenger, B., and J. Cuxart, 2017: Evening transition by a river sampled using a remotely-piloted
889 multicopter. *Bound.-Layer Meteor.*, doi:10.1007/s10546-017-0291-9.

890 **LIST OF TABLES**

891 **Table 1.** Alphabetic list of campaign participants. 43

892 **Table 2.** Specifications of the AWS instrumentation with measured parameters: tem-
 893 perature, T ; sonic temperature, T_s ; relative humidity, RH; pressure, p ; wind
 894 components, u , v , w ; wind speed, ws; wind direction, wd; cloud base height,
 895 h_{CB} and fraction CF; SYNOP weather codes, syn; precipitation, prec; visibil-
 896 ity, vis, H_2O and CO_2 concentration; up and downwelling short and longwave
 897 radiation, $SW^{\uparrow\downarrow}$, $LW^{\uparrow\downarrow}$; ground heat flux, GF. 44

898 **Table 3.** Remote sensing systems specifications with measured parameters as in Table 2
 899 and radial wind speed, u_{rad} ; standard deviation of wind velocity components,
 900 σu , σv , σw ; attenuated backscatter signal strength, bsc; carrier to noise ratio,
 901 CNR. 45

902 **Table 4.** UAS specifications with measured parameters as in Table 2 and infra-red tem-
 903 perature, T_{IR} . In addition to the listed sensors each UAS is equipped with a
 904 GNSS to measure the aircraft’s position (latitude, lat; longitude, lon; altitude,
 905 alt) and an IMU for the aircraft’s attitude angles (pitch θ ; roll, ϕ ; yaw, ψ). See
 906 listed references for more detailed information. 46

907 **Table 5.** List of IOPs during ISOBAR17 and ISOBAR18, summarizing the observed
 908 ABL conditions (i.e., stability regime; wind regime; relevant phenomena; and
 909 maximum near-surface vertical temperature difference and lapse rate) and the
 910 corresponding large-scale conditions (i.e., average wind speed and direction
 911 (850 hPa to 925 hPa); subsidence ($\bar{\omega}$); horizontal temperature-advection (adv);
 912 cloud cover; and synoptic situation). Additional information on the evolution
 913 of the large-scale conditions is given in parentheses. The large-scale conditions
 914 are extracted from ERA5 reanalysis data (Hersbach et al. 2020). 47

915 **Table A1.** List of Abbreviations 49

TABLE 1. Alphabetic list of campaign participants.

Name	Affiliation	Year
Jan Ahrens	Ostwestfalen-Lippe UASA	2018
Kjell zum Berge	University of Tübingen	2018
Elise Mogster Braaten	University of Bergen	2018
Line Båserud	University of Bergen	2017/2018
Phil Chilson	University of Oklahoma	2018
Ewan O'Connor	Finnish Meteorological Institute	2017
William Doyle	University of Oklahoma	2018
Heidi Midtgarden Golid	University of Bergen	2018
Brian Greene	University of Oklahoma	2018
Kristine Flacké Haualand	University of Bergen	2018
Philipp Hilsheimer	University of Tübingen	2017
Marie Hundhausen	University of Tübingen	2017
Stephan T. Kral	University of Bergen	2017/2018
Marius O. Jonassen	University Centre in Svalbard	2017
Carsten Langohr	Ostwestfalen-Lippe UASA	2017/2018
Christian Lindenberg	Lindenberg und Müller GmbH & Co. KG	2017/2018
Patrick Manz	University of Tübingen	2018
Hasan Mashni	University of Tübingen	2018
Santiago Mazuera	University of Oklahoma	2018
Martin Müller	Lindenberg und Müller GmbH & Co. KG	2017/2018
Elizabeth Pillar-Little	University of Oklahoma	2018
Alexander Rautenberg	University of Tübingen	2017/2018
Joachim Reuder	University of Bergen	2018
Martin Schön	University of Tübingen	2018
Markus Schygulla	University of Tübingen	2017
Antonio Segalés	University of Oklahoma	2018
Andrew Seidl	University of Bergen	2018
Irene Suomi	Finnish Meteorological Institute	2017/2018
Gabin H. Urbancic	University of Bergen	2017
Timo Vihma	Finnish Meteorological Institute	2017/2018
Hendrik Voss	Ostwestfalen-Lippe UASA	2017/2018
Burkhard Wrenger	Ostwestfalen-Lippe UASA	2017/2018

916 TABLE 2. Specifications of the AWS instrumentation with measured parameters: temperature, T ; sonic
917 temperature, T_s ; relative humidity, RH; pressure, p ; wind components, u , v , w ; wind speed, ws; wind direction,
918 wd; cloud base height, h_{CB} and fraction CF; SYNOP weather codes, syn; precipitation, prec; visibility, vis, H_2O
919 and CO_2 concentration; up and downwelling short and longwave radiation, $SW^{\uparrow\downarrow}$, $LW^{\uparrow\downarrow}$; ground heat flux, GF.

AWS	Parameters	Sensor	Acq. Period	Meas. Height
FMI (2017/18) @65.0399 °N, 24.5592 °E	T , RH	Vaisala HMP155	10 min	2.0 magl (9 masl)
	p	Vaisala PTB 201A	10 min	7 masl
	T	Pentronic AB Pt100	10 min	2.0 magl (9 masl)
	ws, wd, T_s	Adolf Thies UA2D	1 s	38.5 magl (45.5 masl)
	h_{CB} , CF	Vaisala CT25K Laser Ceilometer	10 min	
	syn, prec, vis	Vaisala FD12P Weather Sensor	10 min	
GFI (2017) @65.0378 °N, 24.5549 °E	T	Campbell ASPTC (aspirated)	1 min	1.0, 2.0, 4.0 magl
	T	PT100 (aspirated)	1 min	1.0, 2.0, 4.0 magl
	RH	Rotronic HC2-S (aspirated)	1 min	1.0, 2.0, 4.0 magl
	ws	Vector A100LK	1 min	1.0, 2.0, 4.0 magl
	wd	Vector W200P	1 min	1.0, 2.0, 4.0 magl
	$SW^{\uparrow\downarrow}$, $LW^{\uparrow\downarrow}$	Kipp & Zonen CNR1	1 min	1.0 magl
	GF	Hukseflux HFP01	1 min	snow and ice
	u , v , w , T_s	Campbell CSAT-3	0.05 s	2.7 magl
H_2O , CO_2 , p	LI-COR LI7500	0.05 s	2.7 magl	
GFI1 (2018) @65.0365 °N, 24.5548 °E	T	Campbell ASPTC (aspirated)	1 s	2.0 magl
	$SW^{\uparrow\downarrow}$, $LW^{\uparrow\downarrow}$	Kipp & Zonen CNR1	1 s	1.0 magl
	u , v , w , T_s	Campbell CSAT-3	0.05 s	2.0 magl
	H_2O , CO_2 , p	LI-COR LI7500	0.05 s	2.0 magl
GFI2 (2018) @65.0360 °N, 24.5556 °E	T	Campbell ASPTC (aspirated)	1 s	0.6, 2.0, 6.8 magl
	T	PT100 (aspirated)	1 s	0.6, 2.0, 6.8 magl
	RH	Rotronic HC2-S (aspirated)	1 s	0.6, 2.0, 6.8 magl
	ws	Vector A100LK	1 s	0.6, 2.0, 6.8 magl
	wd	Vector W200P	1 s	0.6, 2.0, 6.8 magl
	$SW^{\uparrow\downarrow}$, $LW^{\uparrow\downarrow}$	Kipp & Zonen CNR1	1 s	6.4 magl
	GF	Hukseflux HFP01	snow and ice	
	u , v , w , T_s	Campbell CSAT-3	0.05 s	2.0, 4.6, 10.3 magl
H_2O , CO_2 , p	LI-COR LI7500	0.05 s	2.0 magl	

920 TABLE 3. Remote sensing systems specifications with measured parameters as in Table 2 and radial wind speed, u_{rad} ; standard deviation of wind
 921 velocity components, σu , σv , σw ; attenuated backscatter signal strength, bsc; carrier to noise ratio, CNR.

Instrument	Type	Parameters	Range	Resolution	Acq. Period
LATAN-3M (2017/18)	1D sodar	w , σw , bsc	10–340 m agl	10 m (vertical)	3 s
WindCube 100S (2017)	3D scanning doppler lidar	u_{rad} , CNR	50–3300 m (radial)	25 m (radial)	1 s
WindCube v1 (2018)	3D doppler lidar	u , v , w , σu , σv , σw , CNR	40–250 m agl	20 m (vertical)	4 s
MFAS (2018)	3D sodar	u , v , w , σw , bsc	40–1000 m agl	10 m (vertical)	10 min

922 TABLE 4. UAS specifications with measured parameters as in Table 2 and infra-red temperature, T_{IR} . In
 923 addition to the listed sensors each UAS is equipped with a GNSS to measure the aircraft’s position (latitude, lat;
 924 longitude, lon; altitude, alt) and an IMU for the aircraft’s attitude angles (pitch θ ; roll, ϕ ; yaw, ψ). See listed
 925 references for more detailed information.

UAS	Operator	Parameter	Sensor	Acq. Freq.	Reference
SUMO (Fixed-wing)	GFI	T , RH	Sensirion SHT75	2 Hz	Reuder et al. (2009)
		T	Pt1000 Heraeus M222	8.5 Hz	Reuder et al. (2012a)
		p	MS 5611	4 Hz	
		T_{IR}	MLX90614	8.5 Hz	
		ws, wd	Aircraft Dynamics	4 Hz	
Bebop2Met (Rotary-wing)	GFI	T , RH	Sensirion SHT75	2 Hz	Kral et al. (2018)
		p	MS 5607	0.77 Hz	
		ws, wd	Aircraft Dynamics	4 Hz	
Q13a (Rotary-wing)	UOWL	T , RH	HYT 271	10 Hz	Wrenger and Cuxart (2017)
		p	BMP 180	10 Hz	
		ws	Modern Device Wind Sensor Rev. P	10 Hz	
Q13b (Rotary-wing)	UOWL	T , RH	HYT 271	10 Hz	Wrenger and Cuxart (2017)
		T	K-type thermocouple 25 μ m	10 Hz	
		p	BMP 180	10 Hz	
		T_{IR}	MLX90614	10 Hz	
CopterSonde (Rotary-wing)	OU	T	iMet XF PT 100	10 Hz	Greene et al. (2019)
		T , RH	HYT 271	10 Hz	Segales et al. (2020)
		p	Pixracer barometer	10 Hz	
		ws, wd	Aircraft Dynamics	10 Hz	
MASC-2/3 (Fixed-wing)	UT	T	Pt-fine-wire	100 Hz	Wildmann et al. (2014)
		T , RH	Sensirion SHT31	10 Hz	Rautenberg et al. (2019)
		RH	P14 Rapid	10 Hz	
		p	HCA-BARO	100 Hz	
		u , v , w	custom 5-hole probe	100 Hz	

926 **TABLE 5.** List of IOPs during ISOBAR17 and ISOBAR18, summarizing the observed ABL conditions (i.e., stability regime; wind regime; relevant
927 phenomena; and maximum near-surface vertical temperature difference and lapse rate) and the corresponding large-scale conditions (i.e., average wind
928 speed and direction (850 hPa to 925 hPa); subsidence ($\overline{\omega}$); horizontal temperature-advection (adv); cloud cover; and synoptic situation). Additional
929 information on the evolution of the large-scale conditions is given in parentheses. The large-scale conditions are extracted from ERA5 reanalysis data
930 (Hersbach et al. 2020).

IOP	Start date		End date		Boundary-layer		Large-scale		No. UAS flights
	No.	time UTC	No.	time UTC	conditions	conditions	conditions		
1	14 Feb 2017	15 Feb 2017	15 Feb 2017	15 Feb 2017	near-neutral to very stable;	6 (11–4) m s^{-1} NNW(NNW–WSW); $\overline{\omega} = 0.07 \text{ Pa s}^{-1}$ adv = 0.01 K h^{-1} ; broken cloud cover; high pressure ridge	15		
	1500	0630	0630	light to calm winds; $\Delta T_{4m-1m} = 3.8 \text{ K}$ ($\Lambda = 1.3 \text{ K m}^{-1}$)					
2	20 Feb 2017	21 Feb 2017	21 Feb 2017	0600	near-neutral; moderate winds;	10(9–11) m s^{-1} NNW; $\overline{\omega} = 0.07 \text{ Pa s}^{-1}$; adv = 0.13 K h^{-1} ; clear sky; weak eastward-propagating trough	13		
	2300	0600	$\Delta T_{4m-1m} = 0.8 \text{ K}$ ($\Lambda = 0.3 \text{ K m}^{-1}$)						
3	21 Feb 2017	21 Feb 2017	21 Feb 2017	2300	partially very stable;	10(6–18) m s^{-1} SSW(NW–S); $\overline{\omega} = 0.02 \text{ Pa s}^{-1}$; adv = -0.06 K h^{-1} ; scattered clouds; weak eastward-propagating trough	9		
	1700	2300	calm to light winds; $\Delta T_{4m-1m} = 6.4 \text{ K}$ ($\Lambda = 2.1 \text{ K m}^{-1}$)						
4	25 Feb 2017	25 Feb 2017	25 Feb 2017	1100	near-neutral; moderate winds;	13(14–12) m s^{-1} NNW; $\overline{\omega} = 0 \text{ Pa s}^{-1}$; adv = 0.56 K h^{-1} ; clear sky; low pressure influence	24		
	0400	1100	$\Delta T_{4m-1m} = 0.5 \text{ K}$ ($\Lambda = 0.2 \text{ K m}^{-1}$)						
5	26 Feb 2017	26 Feb 2017	26 Feb 2017	0730	near-neutral to weakly stable;	6(9–4) m s^{-1} NNW; $\overline{\omega} = 0.01 \text{ Pa s}^{-1}$; adv = -0.12 K h^{-1} ; scattered clouds; weak trough	23		
	0200	0730	moderate winds; rapid-cooling ($\sim 10 \text{ K}$ in 3 h); $\Delta T_{4m-1m} = 0.3 \text{ K}$ ($\Lambda = 0.1 \text{ K m}^{-1}$)						
6	26 Feb 2017	27 Feb 2017	27 Feb 2017	0200	near-neutral to very stable;	5(6–4) m s^{-1} NNE; $\overline{\omega} = 0.08 \text{ Pa s}^{-1}$; adv = 0.16 K h^{-1} ; clear sky; weak pressure gradients	32		
	1400	0200	light to calm winds; wave breaking (Kelvin-Helmholtz billows); $\Delta T_{4m-1m} = 6.2 \text{ K}$ ($\Lambda = 2.1 \text{ K m}^{-1}$)						

7	10 Feb 2018 1130	11 Feb 2018 0100	near-neutral to weakly stable; moderate winds; $\Delta T_{6,9m-0.6m} = 3.2 \text{ K}$ ($\Lambda = 0.5 \text{ K m}^{-1}$)	$13(17-8) \text{ m s}^{-1}$ SW; $\overline{w} = -0.06 \text{ Pa s}^{-1}$; adv = 0.47 K h^{-1} ;	13
8	16 Feb 2018 0500	17 Feb 2018 0400	near-neutral to weakly stable; elevated inversion > 50m; LLJ; $\Delta T_{6,9m-0.6m} = 1.5 \text{ K}$ ($\Lambda = 0.2 \text{ K m}^{-1}$)	$2(4-1) \text{ m s}^{-1}$ S(SE-SW); $\overline{w} = 0.06 \text{ Pa s}^{-1}$; adv = 0.05 K h^{-1} ;	28
9	17 Feb 2018 1400	18 Feb 2018 0230	weakly to very stable; light to calm winds; $\Delta T_{6,9m-0.6m} = 5.6 \text{ K}$ ($\Lambda = 0.9 \text{ K m}^{-1}$)	broken cloud cover; weak pressure ridge	
			$2(3-2) \text{ m s}^{-1}$ NE; $\overline{w} = 0.01 \text{ Pa s}^{-1}$; adv = 0.01 K h^{-1} ;	clear sky to overcast; weak high pressure ridge	38
10	18 Feb 2018 1330	19 Feb 2018 0230	weakly to very stable; very light to calm winds; LLJ (upside-down mixing); wave breaking; $\Delta T_{6,9m-0.6m} = 5.1 \text{ K}$ ($\Lambda = 0.8 \text{ K m}^{-1}$)	$5(4-6) \text{ m s}^{-1}$ NNE; $\overline{w} = 0.03 \text{ Pa s}^{-1}$; adv = -0.23 K h^{-1} ;	45
			overcast, intermittent clear sky periods; high pressure influence (developing)		
11	19 Feb 2018 1500	19 Feb 2018 2200	weakly stable; moderate winds; LLJ; $\Delta T_{6,9m-0.6m} = 3.5 \text{ K}$ ($\Lambda = 0.5 \text{ K m}^{-1}$)	$6(8-5) \text{ m s}^{-1}$ ENE; $\overline{w} = 0.1 \text{ Pa s}^{-1}$; adv = 0.15 K h^{-1} ;	14
			clear sky; high pressure influence		
12	20 Feb 2018 1100	21 Feb 2018 0600	near-neutral to very stable; light winds; elevated inversion 100 m to 180 m; $\Delta T_{6,9m-0.6m} = 5.4 \text{ K}$ ($\Lambda = 0.9 \text{ K m}^{-1}$)	$2(2-3) \text{ m s}^{-1}$ N(NE-NW); $\overline{w} = 0.01 \text{ Pa s}^{-1}$; adv = 0.01 K h^{-1} ;	51
			overcast, clear sky after 0400; high pressure influence		
13	22 Feb 2018 0500	22 Feb 2018 1800	near-neutral to weakly stable; light winds $\Delta T_{6,9m-0.6m} = 2.1 \text{ K}$ ($\Lambda = 0.3 \text{ K m}^{-1}$)	$6(5-7) \text{ m s}^{-1}$ N $\overline{w} = -0.06 \text{ Pa s}^{-1}$; adv = 0.19 K h^{-1} ;	9
			broken cloud cover; clear sky after 1200; high pressure influence		
14	23 Feb 2018 1300	24 Feb 2018 0600	weakly to very stable; light winds; LLJ; waves; $\Delta T_{6,9m-0.6m} = 4.3 \text{ K}$ ($\Lambda = 0.7 \text{ K m}^{-1}$)	$6(6-5) \text{ m s}^{-1}$ NE; $\overline{w} = 0.14 \text{ Pa s}^{-1}$; adv = -0.17 K h^{-1} ;	44
			clear sky, intermittent scattered cloud cover; high pressure influence		

Table A1. List of Abbreviations

AMOR Q13	Advanced Mission and Operation Research Quadcopter (13-inch propellers)
B2M	Bebop2Met
CS	CopterSonde
EC	Eddy-Covariance
ECMWF-IFS	ECMWF Integrated Forecasting System
FMI	Finnish Meteorological Institute
GFI	Geophysical Institute, University of Bergen
ISOBAR	Innovative Strategies for Observations in the Arctic Atmospheric Boundary Layer
lidar	Light Detection and Ranging
LLJ	Low-Level Jet
MASC	Multi-Purpose Airborne Sensor Carrier
MEPS	MetCoOp Ensemble Prediction System
MFAS	Medium Size Flat Array Sodar
MOST	Monin-Obukhov Similarity Theory
OU	University of Oklahoma
QA/QC	Quality Assurance and Quality Check

RRTMG	Rapid Radiative Transfer Model Global
SBL	Stable Boundary Layer
SCM	Single-Column Model
sodar	Sound Detection and Ranging
SUMO	Small Meteorological Observer
UAS	Unmanned Aircraft System
UOWL	Ostwestfalen-Lippe UASA
UT	University of Tübingen
VSBL	Very Stable Boundary Layer
WCv1	Windcube v1
WC100S	Windcube 100S
WSBL	Weakly Stable Boundary Layer

931 **LIST OF FIGURES**

932 **Fig. 1.** Overview maps showing the ISOBAR field site: The two inlay maps at the top display the
933 area of Northern Europe (left) and around Hailuoto and Oulu (right). The large map is based
934 on a Sentinel-2 L2A satellite image from 18 Feb 2019 ([https://apps.sentinel-hub.com/](https://apps.sentinel-hub.com/eo-browser)
935 [eo-browser](https://apps.sentinel-hub.com/eo-browser)) 53

936 **Fig. 2.** The different UAS systems used during the two campaigns. The numbers of flights are
937 indicated in parentheses for ISOBAR17 and ISOBAR18, respectively. 54

938 **Fig. 3.** Data availability for the measurement systems during the ISOBAR17 and ISOBAR18 cam-
939 paigns. For the profiling systems the data availability is given as a function of height.
940 55

941 **Fig. 4.** Overview of the meteorological and sea-ice conditions during the two campaigns in February
942 2017 and 2018. The first and third rows show the time series of temperature, cloud cover,
943 wind speed and direction and pressure observed by the WMO weather station (FMI) during
944 February 2017 and 2018, respectively. The ice charts in the second and fourth rows represent
945 the extrema of the ice coverage during the corresponding period based on data provided by
946 the Finnish Meteorological Institute. Black dotted lines indicate the time of observation and
947 the corresponding location on the maps. 56

948 **Fig. 5.** Combined temperature, T , and wind speed, ws , profiles based on mast, UAS and remote
949 sensing (wind only) data, observed between 1510 and 1530 UTC 23 Feb 2018. Solid lines
950 and shaded areas indicate the mean and standard deviation (bin-averaged for all UAS and
951 time-averaged for ground based systems), respectively. The observation period for the ground
952 based systems is given in the title, the slightly shorter periods for the UAS flights are given
953 in the legends. 57

954 **Fig. 6.** Series of (a) UAS boundary layer profiles and (b) corresponding time series of surface based
955 measurements of T (contours) and ws (wind barbs), observed during IOP-14, 1615 to 2130
956 UTC 23 Feb 2018. The UAS flight times for the data presented in the top panel (ascent up
957 to 250 m) are indicated by shades and additional markers in the bottom panel, applying the
958 corresponding color scheme. 58

959 **Fig. 7.** Time series of various atmospheric parameters during IOP-10, 18-19 Feb 2018: (a) T
960 (observed by GFI2 and FMI); (b) ws (GFI2, FMI and WCv1); (c) sodar attenuated backscatter,
961 bsc , profiles (LATAN-3M); (d) composite profiles of T (UAS, GFI2) and horizontal wind
962 (SUMO, WCv1, MFAS). Magenta boxes indicate the periods of interest analyzed in the
963 following figures. 59

964 **Fig. 8.** Time series of various atmospheric parameters during IOP-10, 1330 to 1615 UTC 18 Feb
965 2018: (a) T (observed by GFI2 and FMI); (b) ws (GFI2, FMI and WCv1); (c) wd (GFI2,
966 FMI and WCv1); (d) vertical velocity perturbation, w' (GFI2, WCv1); (e) instantaneous
967 kinematic heat flux, $\overline{w'T'}$ (GFI2); (f) vertical profiles of T (UAS); (g) vertical profiles of ws
968 (GFI2, WCv1). w' and $\overline{w'T'}$ data are shifted by increments of 0.5 ms^{-1} and 0.25 Kms^{-1} ,
969 respectively, to reveal structures. 60

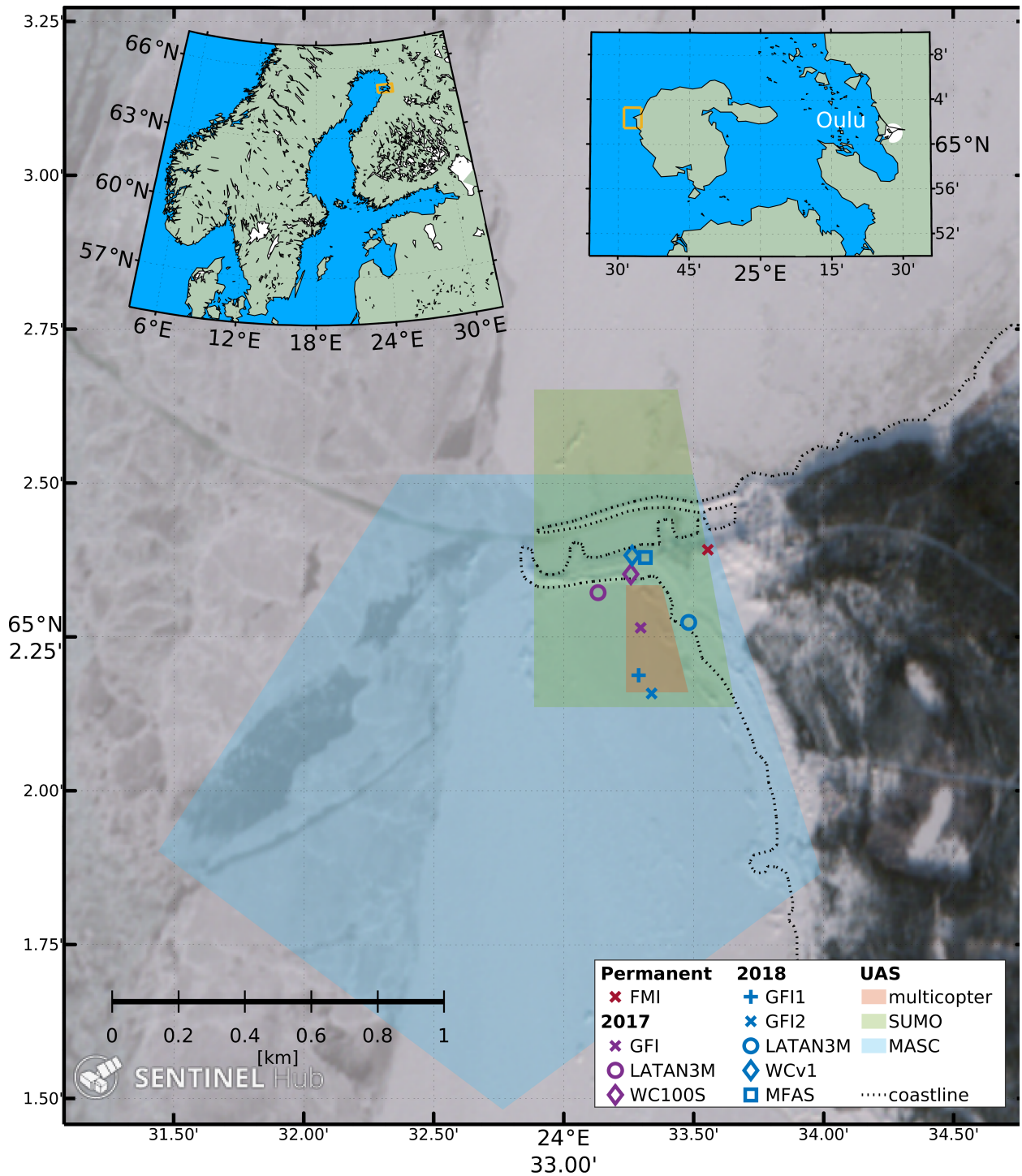
970 **Fig. 9.** Time series of various atmospheric parameters during IOP-10, 2210 to 2245 UTC 18 Feb
971 2018: (a) temperature, T , (contours) and wind speed and direction (wind barbs), observed
972 by GFI2; (b) vertical velocity perturbation, w' (GFI2, WCv1); (c) wind shear, S (GFI2);
973 (d) Richardson number, Ri (GFI2). The w' data are shifted by increments of 0.25 ms^{-1} to

974 reveal structures. Wind speed at all levels and w' data at the upper two levels are smoothed
975 applying a 1-min sliding mean average. T , S , and Ri data are 10-s sliding mean averages. . . . 61

976 **Fig. 10.** Time series of various atmospheric parameters during IOP-10, 2300 UTC 18 Feb 2018 to
977 0100 UTC 19 Feb 2018. (a) temperature (observed by GFI2 and FMI); (b) wind speed (GFI2,
978 FMI and WCv1); (c) wind direction (GFI2, FMI and WCv1); (d) vertical velocity (GFI2,
979 WCv1); (e) instantaneous kinematic heat flux (GFI2); (f) sodar attenuated backscatter profiles
980 (LATAN-3M). The vertical velocity and kinematic heat flux data are shifted by increments
981 of 0.5 m s^{-1} and 0.25 K m s^{-1} respectively, to reveal structures. 62

982 **Fig. 11.** Observations of: (a) UAS profiles of potential temperature and corresponding lidar wind
983 speed profiles; (b) resulting profiles of Ri ; (c) time–height diagram of lidar wind speed; and
984 (d) wavelet energy of 10-m sonic vertical velocity component during IOP-10, 2330 UTC 18
985 Feb 2018 to 0130 UTC 19 Feb 2018. The black dotted line in (b) indicates $Ri = 0.25$. The
986 UAS flight times from (a) and (b) are indicated as vertical lines in the same color in (c) and (d). 63

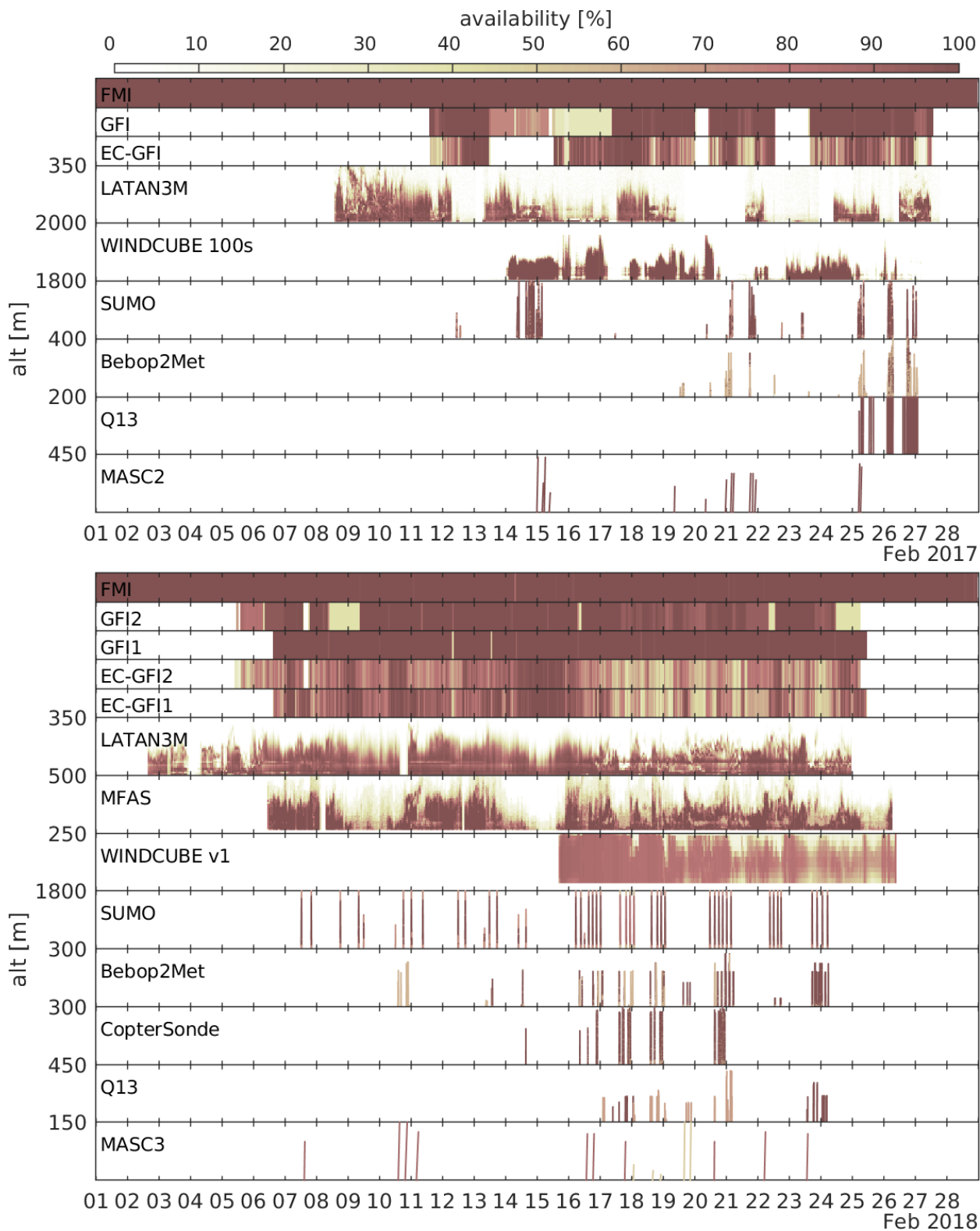
987 **Fig. 12.** Time–height plots of potential temperature from the MEPS forecast (MEPS-NWP), the WRF
988 single-column simulation (WRF-SCM) and the PALM LES simulation (PALM-LES). The
989 data cover the lowermost 500 m and the first 24 h at the measurement site. Observations
990 from SUMO, GFI, FMI are superimposed as circles. 64



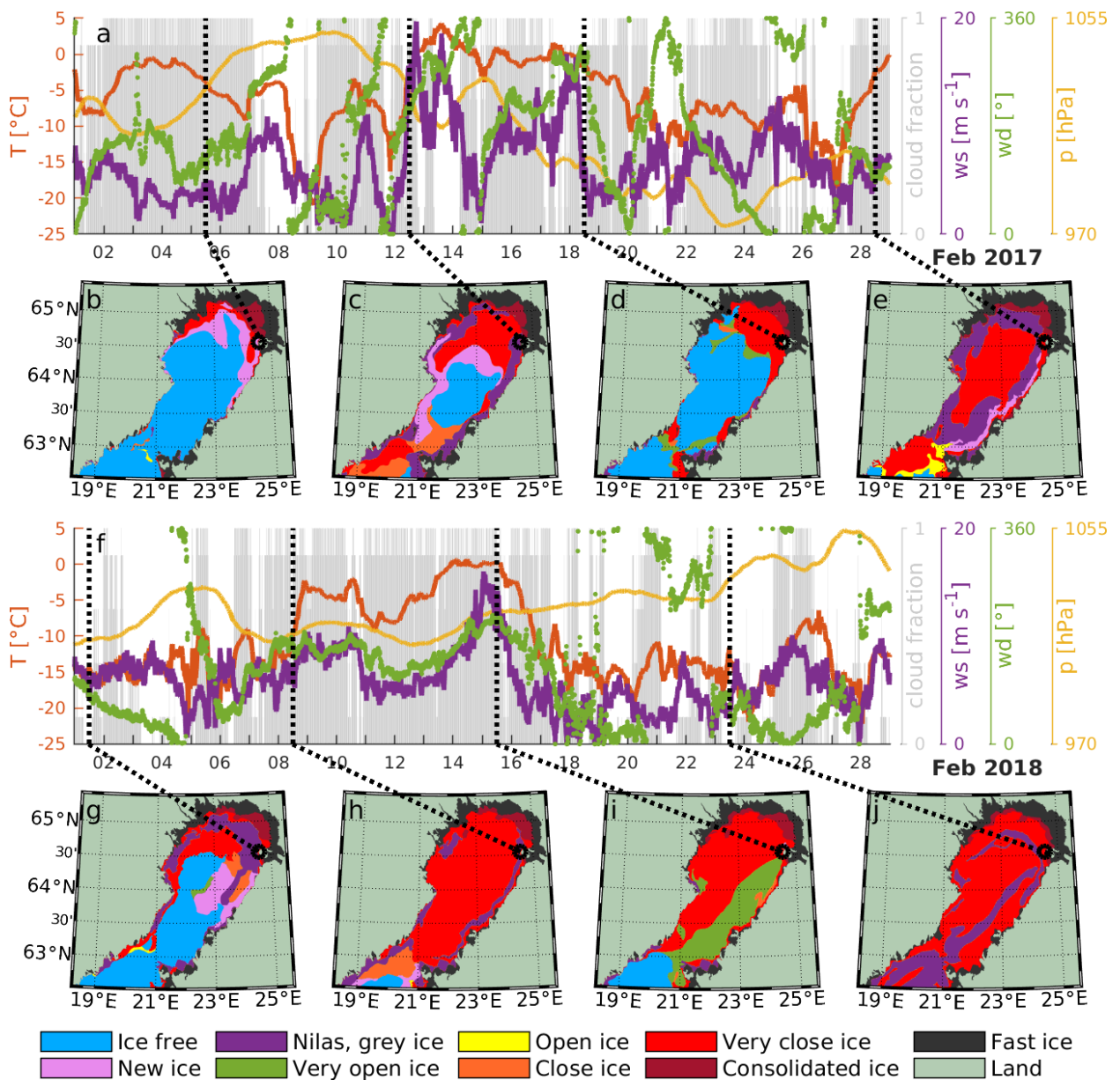
991 FIG. 1. Overview maps showing the ISOBAR field site: The two inlay maps at the top display the area of
 992 Northern Europe (left) and around Hailuoto and Oulu (right). The large map is based on a Sentinel-2 L2A
 993 satellite image from 18 Feb 2019 (<https://apps.sentinel-hub.com/eo-browser>)



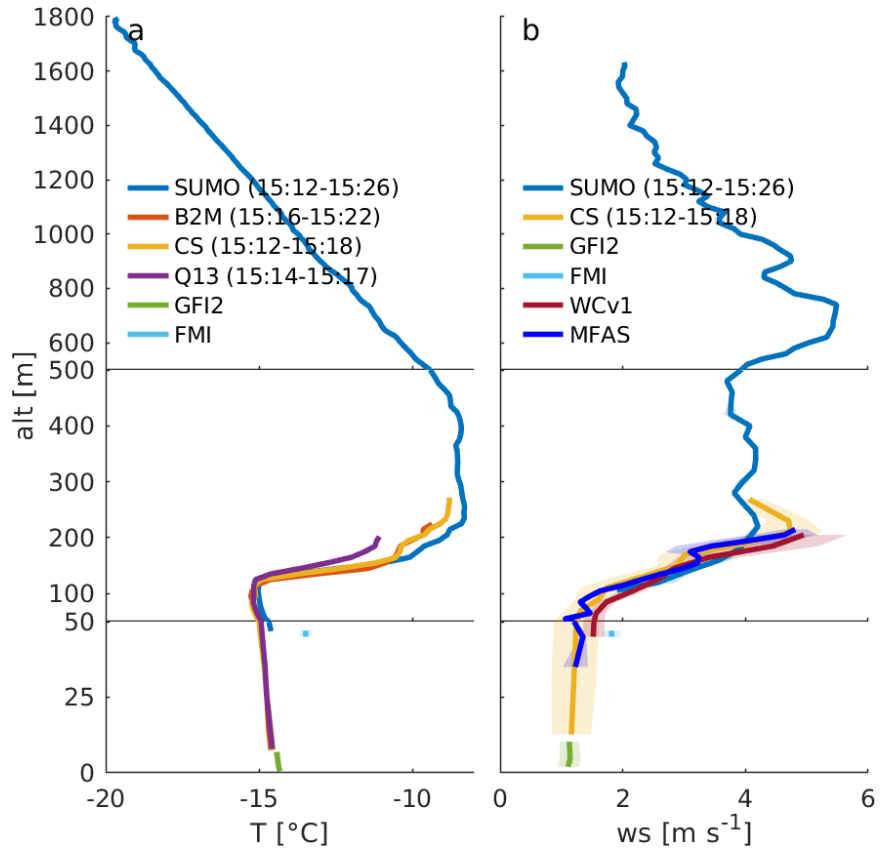
994 FIG. 2. The different UAS systems used during the two campaigns. The numbers of flights are indicated in
 995 parentheses for ISOBAR17 and ISOBAR18, respectively.



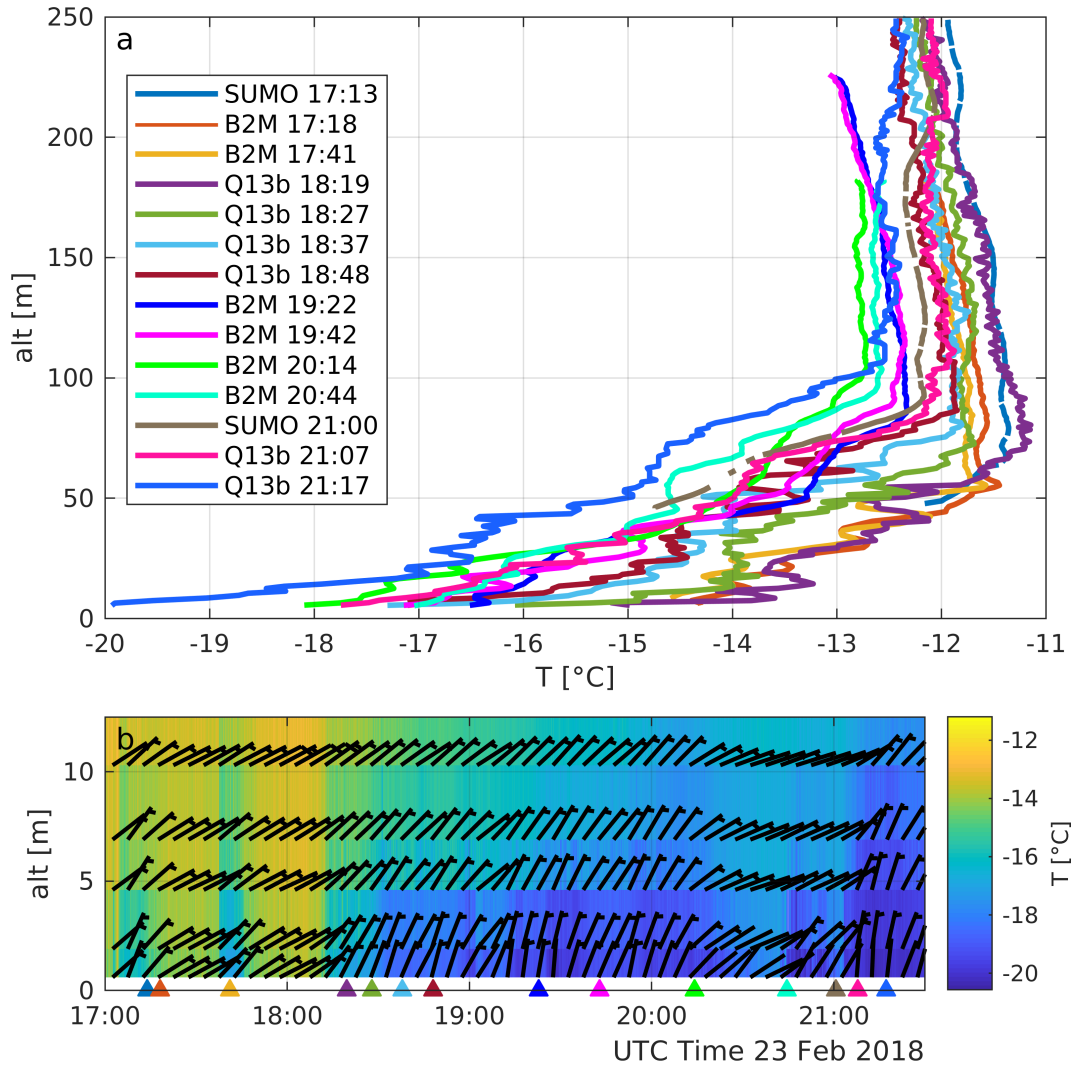
996 FIG. 3. Data availability for the measurement systems during the ISOBAR17 and ISOBAR18 campaigns. For
 997 the profiling systems the data availability is given as a function of height.



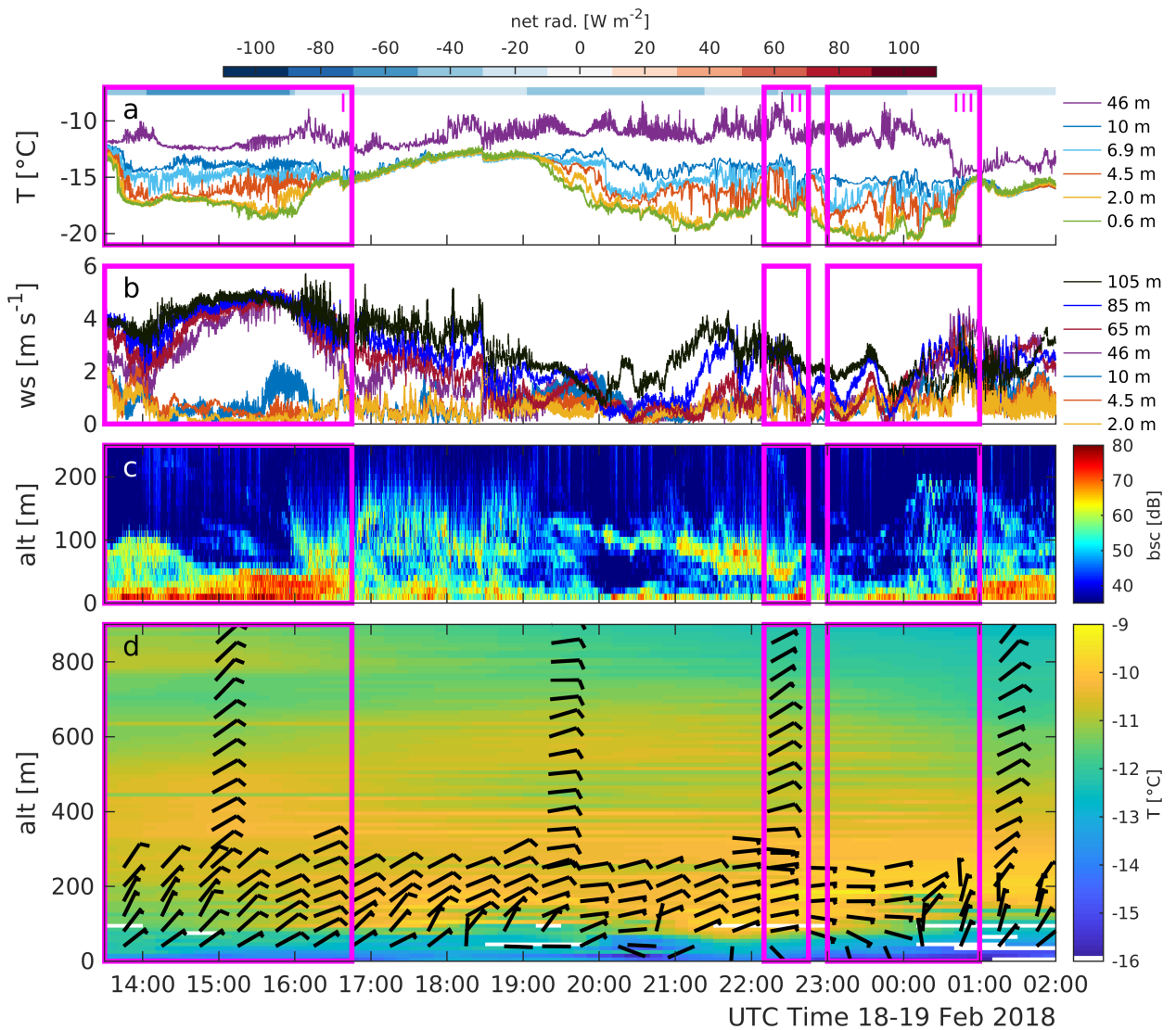
998 FIG. 4. Overview of the meteorological and sea-ice conditions during the two campaigns in February 2017
 999 and 2018. The first and third rows show the time series of temperature, cloud cover, wind speed and direction
 1000 and pressure observed by the WMO weather station (FMI) during February 2017 and 2018, respectively. The
 1001 ice charts in the second and fourth rows represent the extrema of the ice coverage during the corresponding
 1002 period based on data provided by the Finnish Meteorological Institute. Black dotted lines indicate the time of
 1003 observation and the corresponding location on the maps.



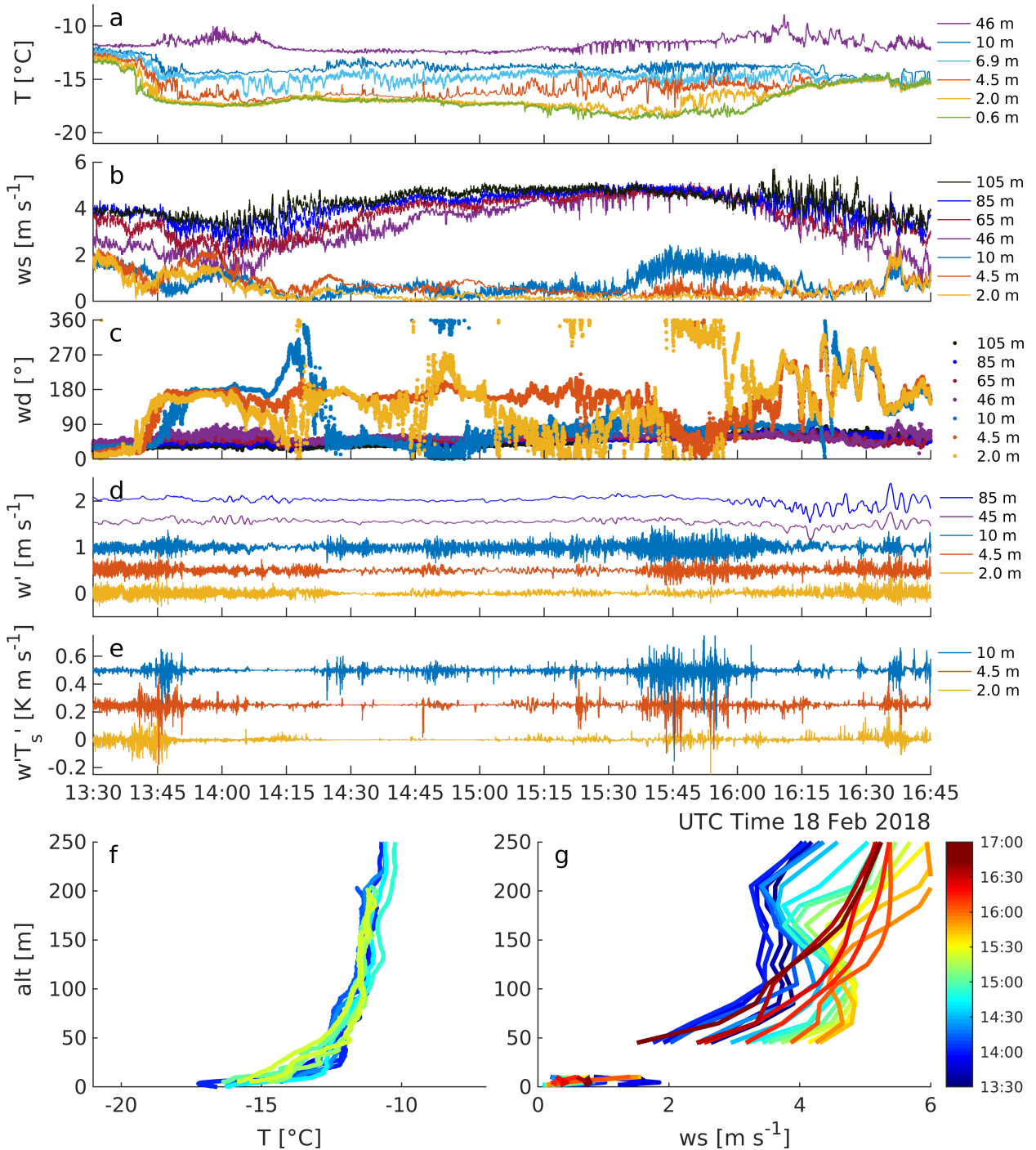
1004 FIG. 5. Combined temperature, T , and wind speed, ws , profiles based on mast, UAS and remote sensing (wind
 1005 only) data, observed between 1510 and 1530 UTC 23 Feb 2018. Solid lines and shaded areas indicate the mean
 1006 and standard deviation (bin-averaged for all UAS and time-averaged for ground based systems), respectively. The
 1007 observation period for the ground based systems is given in the title, the slightly shorter periods for the UAS
 1008 flights are given in the legends.



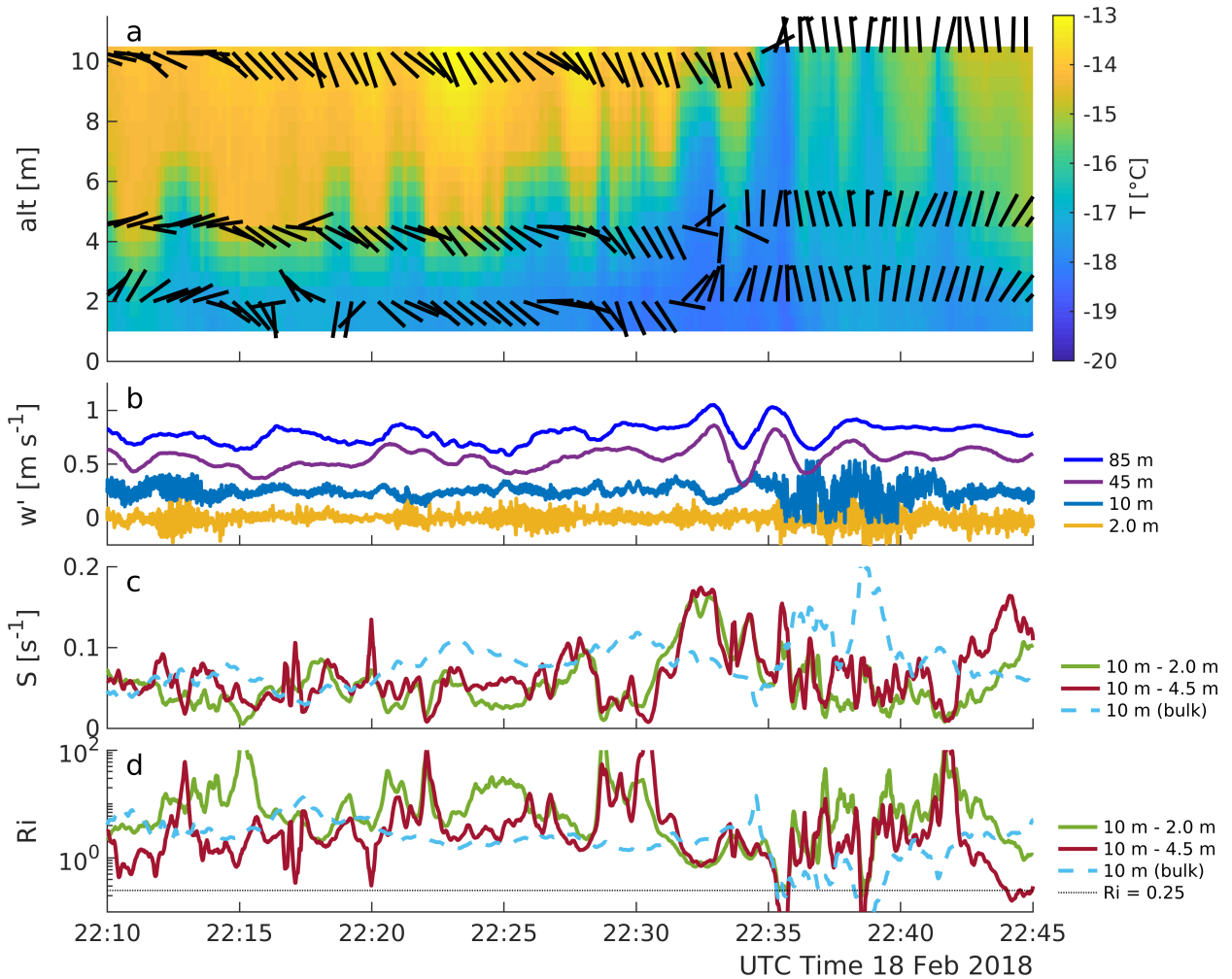
1009 FIG. 6. Series of (a) UAS boundary layer profiles and (b) corresponding time series of surface based measure-
 1010 ments of T (contours) and w_s (wind barbs), observed during IOP-14, 1615 to 2130 UTC 23 Feb 2018. The UAS
 1011 flight times for the data presented in the top panel (ascent up to 250 m) are indicated by shades and additional
 1012 markers in the bottom panel, applying the corresponding color scheme.



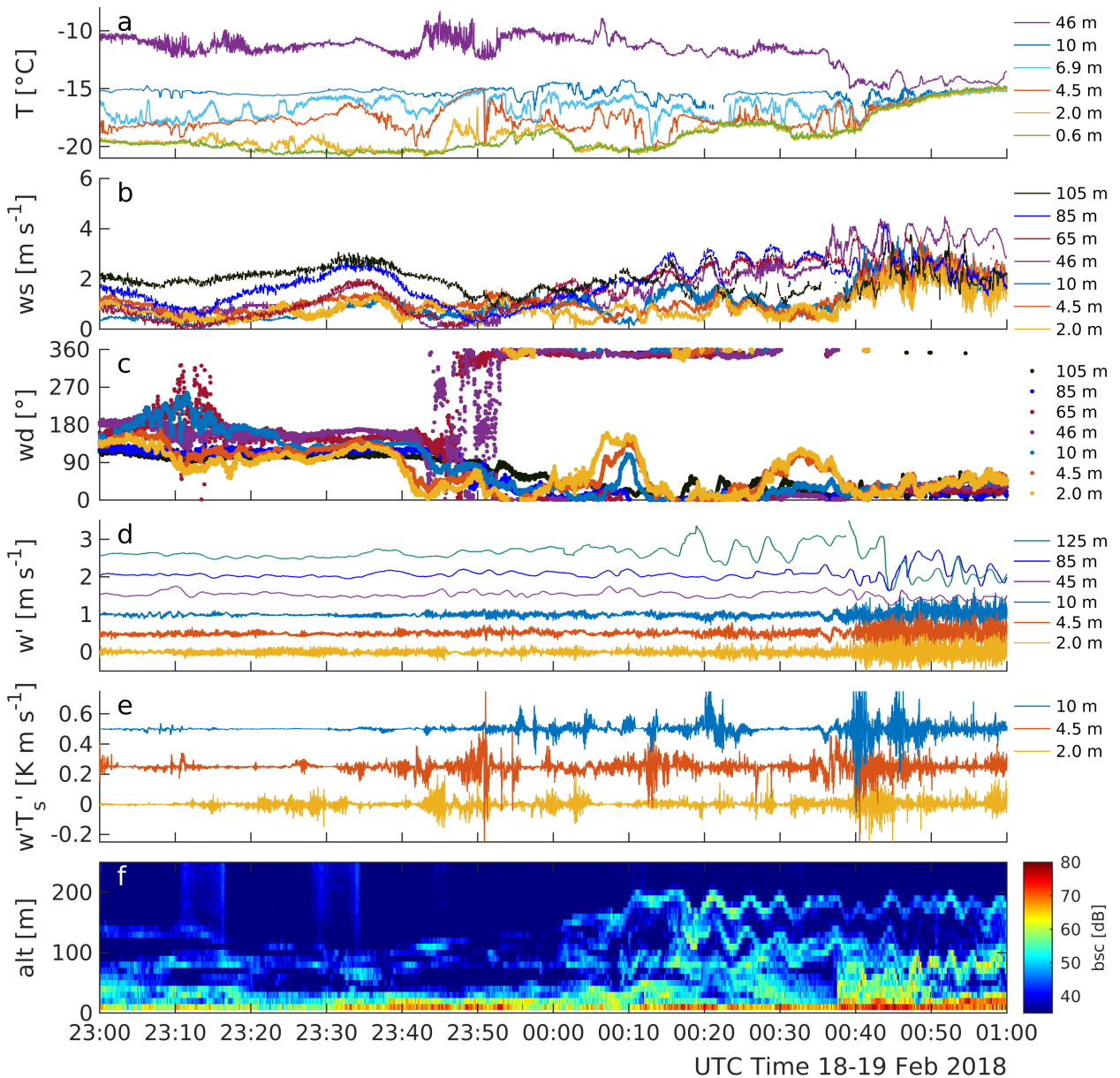
1013 FIG. 7. Time series of various atmospheric parameters during IOP-10, 18-19 Feb 2018: (a) T (observed by
 1014 GFI2 and FMI); (b) ws (GFI2, FMI and WCv1); (c) sodar attenuated backscatter, bsc , profiles (LATAN-3M);
 1015 (d) composite profiles of T (UAS, GFI2) and horizontal wind (SUMO, WCv1, MFAS). Magenta boxes indicate
 1016 the periods of interest analyzed in the following figures.



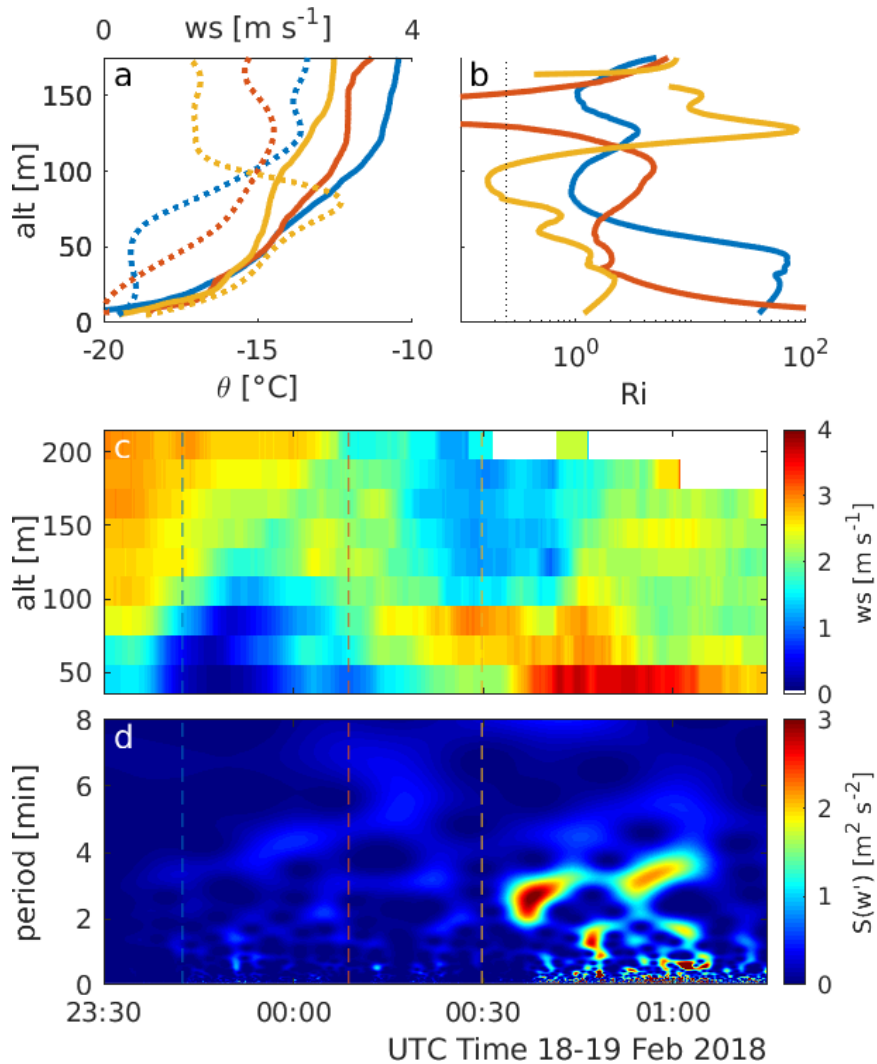
1017 FIG. 8. Time series of various atmospheric parameters during IOP-10, 1330 to 1615 UTC 18 Feb 2018: (a)
 1018 T (observed by GFI2 and FMI); (b) w_s (GFI2, FMI and WCv1); (c) w_d (GFI2, FMI and WCv1); (d)
 1019 vertical velocity perturbation, w' (GFI2, WCv1); (e) instantaneous kinematic heat flux, $\overline{w'T'}$ (GFI2); (f) vertical profiles
 1020 of T (UAS); (g) vertical profiles of w_s (GFI2, WCv1). w' and $\overline{w'T'}$ data are shifted by increments of 0.5 m s^{-1}
 1021 and 0.25 K m s^{-1} , respectively, to reveal structures.



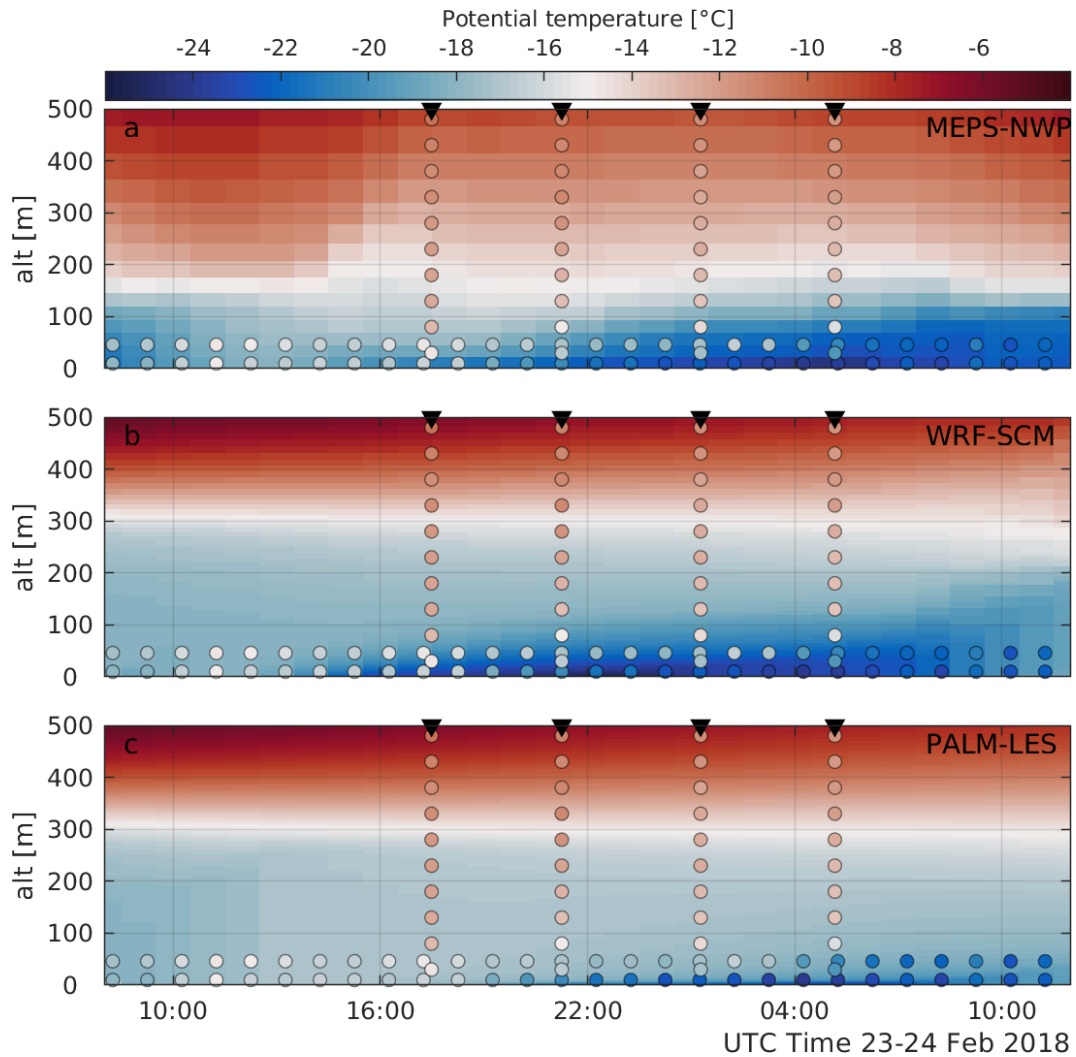
1022 FIG. 9. Time series of various atmospheric parameters during IOP-10, 2210 to 2245 UTC 18 Feb 2018: (a)
 1023 temperature, T , (contours) and wind speed and direction (wind barbs), observed by GFI2; (b) vertical velocity
 1024 perturbation, w' (GFI2, WCv1); (c) wind shear, S (GFI2); (d) Richardson number, Ri (GFI2). The w' data are
 1025 shifted by increments of 0.25 ms^{-1} to reveal structures. Wind speed at all levels and w' data at the upper two
 1026 levels are smoothed applying a 1-min sliding mean average. T , S , and Ri data are 10-s sliding mean averages.



1027 FIG. 10. Time series of various atmospheric parameters during IOP-10, 2300 UTC 18 Feb 2018 to 0100 UTC
 1028 19 Feb 2018. (a) temperature (observed by GFI2 and FMI); (b) wind speed (GFI2, FMI and WCv1); (c) wind
 1029 direction (GFI2, FMI and WCv1); (d) vertical velocity (GFI2, WCv1); (e) instantaneous kinematic heat flux
 1030 (GFI2); (f) sodar attenuated backscatter profiles (LATAN-3M). The vertical velocity and kinematic heat flux
 1031 data are shifted by increments of 0.5 m s^{-1} and 0.25 K m s^{-1} respectively, to reveal structures.



1032 FIG. 11. Observations of: (a) UAS profiles of potential temperature and corresponding lidar wind speed
 1033 profiles; (b) resulting profiles of Ri ; (c) time–height diagram of lidar wind speed; and (d) wavelet energy of 10-m
 1034 sonic vertical velocity component during IOP-10, 2330 UTC 18 Feb 2018 to 0130 UTC 19 Feb 2018. The black
 1035 dotted line in (b) indicates $Ri = 0.25$. The UAS flight times from (a) and (b) are indicated as vertical lines in the
 1036 same color in (c) and (d).



1037 FIG. 12. Time–height plots of potential temperature from the MEPS forecast (MEPS-NWP), the WRF single-
 1038 column simulation (WRF-SCM) and the PALM LES simulation (PALM-LES). The data cover the lowermost
 1039 500 m and the first 24 h at the measurement site. Observations from SUMO, GFI, FMI are superimposed as
 1040 circles.